Long-exposure NuSTAR constraints on decaying dark matter in the Galactic halo

Brandon M. Roach,[1,*] Steven Rossland,[2,†] Kenny C. Y. Ng,[3,‡] Kerstin Perez,[1,§] John F. Beacom,[4,5,6,‖] Brian W. Grefenstette,[7,¶] Shunsaku Horiuchi,[8,9,**] Roman Krivonos,[10,11,††] and Daniel R. Wik[2,‡‡]

[1]*Department of Physics, Massachusetts Institute of Technology, Cambridge, Massachusetts 02139, USA*
[2]*Department of Physics and Astronomy, University of Utah, Salt Lake City, Utah 84112, USA*
[3]*Department of Physics, The Chinese University of Hong Kong, Sha Tin, Hong Kong, China*
[4]*Center for Cosmology and AstroParticle Physics (CCAPP), Ohio State University, Columbus, Ohio 43210, USA*
[5]*Department of Physics, Ohio State University, Columbus, Ohio 43210, USA*
[6]*Department of Astronomy, Ohio State University, Columbus, Ohio 43210, USA*
[7]*Space Radiation Laboratory, California Institute of Technology, Pasadena, California 91125, USA*
[8]*Center for Neutrino Physics, Department of Physics, Virginia Tech, Blacksburg, Virginia 24061, USA*
[9]*Kavli IPMU (WPI), UTIAS, The University of Tokyo, Kashiwa, Chiba 277-8583, Japan*
[10]*Space Research Institute (IKI), Russian Academy of Sciences, Moscow 117997, Russia*
[11]*Institute for Nuclear Research, Russian Academy of Sciences, Moscow 117312, Russia*

(Received 18 August 2022; accepted 16 December 2022; published 13 January 2023)

We present two complementary NuSTAR x-ray searches for keV-scale dark matter decaying to monoenergetic photons in the Milky Way halo. In the first, we utilize the known intensity pattern of unfocused stray light across the detector planes—the dominant source of photons from diffuse sources—to separate astrophysical emission from internal instrument backgrounds using ∼7- Ms/detector deep blank-sky exposures. In the second, we present an updated parametric model of the full NuSTAR instrument background, allowing us to leverage the statistical power of an independent ∼20-Ms/detector stacked exposures spread across the sky. Finding no evidence of anomalous x-ray lines using either method, we set limits on the active-sterile mixing angle $\sin^2(2\theta)$ for sterile-neutrino masses 6–40 keV. The first key result is that we strongly disfavor a ∼7-keV sterile neutrino decaying into a 3.5-keV photon. The second is that we derive leading limits on sterile neutrinos with masses ∼15–18 keV and ∼25–40 keV, reaching or extending below the big bang nucleosynthesis limit. In combination with previous results, the parameter space for the neutrino minimal standard model is now nearly closed.

DOI: 10.1103/PhysRevD.107.023009

I. INTRODUCTION

Nearly a century of cosmological observations have indicated the presence of gravitating degrees of freedom that do not couple to electromagnetism with the same strength as the visible Standard Model (SM) particles. One class of searches for this dark matter (DM, hereafter symbolized χ) is indirect detection, in which astrophysical observatories are used to search for the decay and/or annihilation of DM particles into stable SM particles (see, e.g., Refs. [1–3]). Unlike charged-particle cosmic rays, photons and neutrinos are not scattered by astrophysical magnetic fields, allowing any putative DM signal to be correlated against known astrophysical sources.

A popular DM candidate with a final-state photon signal amenable to indirect detection is the keV-scale sterile neutrino. Models such as the neutrino minimal standard model (νMSM, Refs. [4–7]) incorporate these sterile neutrinos while simultaneously seeking to account for the observed neutrino mass spectrum and the cosmological matter/antimatter asymmetry. Such sterile neutrinos are particularly interesting as a candidate for indirect DM searches, as their radiative decays $\chi \to \gamma\nu_\ell$ to the SM lepton neutrinos ν_ℓ would produce a monoenergetic x-ray line with energy $E_\gamma = m_\chi/2$ and decay rate $\Gamma_{\chi\to\gamma\nu}$ set by m_χ and the active-sterile mixing $\sin^2(2\theta)$. In the early Universe, sterile neutrinos may have been produced via

*roachb@mit.edu
†u1019304@utah.edu
‡kcyng@phy.cuhk.edu.hk
§kmperez@mit.edu
‖beacom.7@osu.edu
¶bwgref@srl.caltech.edu
**horiuchi@vt.edu
††krivonos@cosmos.ru
‡‡wik@astro.utah.edu

oscillation-induced mixing with the SM neutrinos [8], with a primordial lepton asymmetry potentially enhancing the rates [9].

Many space-based x-ray observatories have contributed to the search for radiative sterile-neutrino DM decays [10–30]. These include focusing telescopes such as the Chandra X-ray Observatory (CXO), XMM-Newton, Hitomi, and Suzaku, and nonfocusing instruments such as Halosat, the Fermi Gamma-ray Burst Monitor and the INTEGRAL Soft Photon Imager. The different sensitivity bands of these instruments led to a gap in the mass-mixing angle parameter space for sterile-neutrino masses ∼10–25 keV. Additionally, claims of the detection of an anomalous x-ray line at $E_\gamma \simeq 3.5$ keV ($m_\chi \simeq 7$ keV, Refs. [31,32]) motivate covering the sterile-neutrino DM parameter space with as many instruments, observation targets, and analysis techniques as possible.

The NuSTAR observatory (launched in 2012, Ref. [33]) is uniquely suited to fill in this gap in the mass-mixing-angle parameter space, and to test the origin of the 3.5-keV anomaly. Following a search for sterile-neutrino DM in focused observations of the Bullet cluster [34], subsequent NuSTAR analyses used the so-called 0-bounce (unfocused stray light) photons to derive leading limits on sterile-neutrino decays in blank-sky extragalactic fields [35], the Galactic Center, [36], the M31 galaxy [37], and the Galactic bulge [38], though these analyses were limited by a combination of astrophysical background emission, limited statistics, and systematic deviations from the fiducial instrument background model.

In this paper, we leverage NuSTAR's extensive observational catalog since 2012 to derive robust constraints on $\sin^2(2\theta)$ across much of the 6–40 keV mass range, using two independent datasets and analysis techniques. First, we use the known intensity pattern of unfocused stray light on the NuSTAR detectors to separate astrophysical emission from internal instrument backgrounds using 7-Ms/detector deep blank-sky exposures, which allows us to derive a novel limit on $\sin^2(2\theta)$ for sterile-neutrino masses between 6–40 keV. This technique allows us to greatly suppress instrument backgrounds, and especially to probe the challenging ∼6–10-keV mass range. Second, we apply an improved parametric model of the NuSTAR instrumental and astrophysical backgrounds to the full ∼20-Ms/detector dataset, providing improved sensitivity at higher masses, ∼25–40 keV.

In Sec. II, we briefly describe the aspects of the NuSTAR observatory design relevant to our sterile-neutrino search. In Sec. III, we describe the novel "spatial-gradient" technique that allows us to separate 0-bounce photons from detector backgrounds. In Sec. IV, we discuss the development and implementation of the updated NuSTAR parametric background model. In Sec. V, we scan the NuSTAR spectra from both analysis techniques for evidence of decaying DM, particularly keV-scale sterile neutrinos. We conclude in Sec. VI.

II. NUSTAR AS A DARK-MATTER OBSERVATORY

The aspects of the NuSTAR instrument relevant for sterile-neutrino searches have been described in previous analyses [35–38]; here, we reiterate the most important points.

A. NuSTAR optics modules

NuSTAR carries two coaligned x-ray telescopes labeled A and B, each comprised of an optics module (OM) and a focal plane module (FPM) separated by the observatory's 10-meter carbon-fiber mast. The OMs are conical approximations to the Wolter-I grazing-incidence design, with properly focused x-rays reflecting twice inside the OMs—first against the parabolic mirrors and second against the hyperbolic mirrors—hence their alternative name of "2-bounce" (2b) photons. The multilayer construction of the mirrors with alternating layers of platinum/silicon carbide and tungsten/silicon affords NuSTAR considerable focused area for photon energies E_γ between 3–79 keV. The focused FOV of NuSTAR subtends a solid angle $\Delta\Omega_{2b} = 13' \times 13' \approx 0.047$ deg^2, and the optics provide a maximum FOV-averaged effective area $\langle A_{2b}\rangle \approx 170$ cm^2 per FPM for photon energies $E_\gamma \approx 10$ keV. Thus, the maximum 2-bounce grasp $\langle A_{2b}\Delta\Omega_{2b}\rangle \approx 8$ cm^2 deg^2 per FPM.

B. NuSTAR focal plane modules

At the opposite end of the mast from the optics modules sit the FPMs. Each FPM consists of a solid-state detector array, a cesium iodide anticoincidence shield to veto incoming cosmic rays, a series of three annular aperture stops to block off-axis photons from striking the detectors, and a ∼0.1-mm beryllium window with energy-dependent transmission coefficient $\mathcal{E}_{Be}$ to block lower-energy photons. Each FPM detector array consists of four cadmium zinc telluride (CdZnTe) crystals, with each crystal having dimensions $(20 \times 20 \times 2)$ mm^3 and segmented into a 32×32 grid of $(0.6\text{ mm})^2$ pixels. The detectors have energy resolution ∼0.4 keV FWHM for photon energies $E_\gamma \lesssim 10$ keV, increasing to ∼0.9 keV FWHM at $E_\gamma \approx 80$ keV. The detector response is defined for energies 1.6–164 keV and is divided into 4096 channels of width 40 eV. At present, only the $E_\gamma > 3$ keV response is known with sufficient precision for this study, but work is ongoing to extend to lower energies [39].

Before interacting with the active CdZnTe, photons must pass through the ∼100-nm platinum contact, as well as a ∼200-nm "dead layer" of inactive CdZnTe. The thickness of these layers vary somewhat between individual detector chips, calibrated using extensive off-axis observations of the Crab nebula [40,41]. We incorporate the energy-dependent throughput of the platinum contact and CdZnTe dead layer into an overall transmission coefficient $\mathcal{E}_{det}$.

C. The 0-bounce technique

Unlike previous focusing x-ray observatories such as CXO or XMM-Newton, the path between the NuSTAR optics bench and the detector plane is largely open to the sky. This configuration allows photons with off-axis angles ∼1–3° to strike the detectors without being focused by the mirror optics, hence their name "0-bounce" (0b) photons. The effective 0-bounce solid angle $\Delta\Omega_{0b} \equiv \int_{FOV} \xi_{0b}\, d\Omega$ is determined by the geometry of the aperture stops within the FPMs, partially blocked by the optics bench to form a crescent "Pac-Man" gradient in efficiency ξ_{0b} across the detectors (see, e.g., Refs. [36,42,43] for a schematic). Since these 0-bounce photons bypass the focusing optics, the unfocused effective area A_{0b} is limited by the physical ∼13 cm^2 area of each detector array. The usable area of each detector chip ranges between 3.12–3.19 cm^2 due to the varying amount of "bad pixels" flagged in the Calibration Database (CALDB). As detector arrays A/B have different orientations with respect to the optics bench, the 0-bounce efficiency and effective solid angle $\Delta\Omega_{0b}$ vary across the detector chips, and between FPMA and FPMB. Taking $\Delta\Omega_{0b} \approx 4.5$ deg^2 as the approximate solid angle for each FPM, the 0-bounce grasp $\langle A_{0b}\Delta\Omega_{0b}\rangle \approx 55$ cm^2 deg^2 per FPM, nearly an order of magnitude larger than the maximum 2-bounce grasp. Additionally, unlike the 2-bounce grasp, the 0-bounce grasp is essentially constant for $E_\gamma \gtrsim 10$ keV. These 0-bounce photons are ideal for studies of diffuse x-rays on ∼degree scales, e.g., dark matter decay.

D. Expected DM signal

With the NuSTAR instrument responses in hand, we may readily calculate the expected DM-decay-induced photon intensity $\mathcal{I}_{DM} \equiv d^2F_\gamma/dE_\gamma d\Omega$ at the telescope:

$$\begin{aligned}\mathcal{I}_{DM} &= \frac{\Gamma}{4\pi m_\chi}\frac{dN}{dE_\gamma}\left[\frac{1}{\Delta\Omega}\int_{FOV}\xi\, d\Omega\int_{LOS}\rho_\chi ds\right],\\ &= \frac{\Gamma}{4\pi m_\chi}\frac{dN}{dE_\gamma}\left[\frac{1}{\Delta\Omega}\int_{FOV}\xi\frac{d\mathcal{D}}{d\Omega}d\Omega\right],\\ &= \frac{\Gamma}{4\pi m_\chi}\frac{dN}{dE_\gamma}\left\langle\frac{d\mathcal{D}}{d\Omega}\right\rangle. \end{aligned} \quad (1)$$

Here, Γ is the decay rate to some final state with associated photon spectrum dN/dE_γ, the latter being normalized to the number of final-state photons in that channel. For the two-body final states with $m_x \ll m_\chi$ considered in this work (i.e., $\chi \to \gamma x$) and assuming the linewidth is much less than the ∼0.4-keV FWHM detector energy resolution, $dN/dE_\gamma \simeq \delta(E_\gamma - m_\chi/2)$. The term in square brackets is the FOV-averaged DM column density per solid angle $\langle d\mathcal{D}/d\Omega\rangle$, where $\Delta\Omega = \int_{FOV}\xi d\Omega$ is the effective solid angle for the 0-bounce or 2-bounce FOV, as appropriate, and s is the distance along the line of sight (LOS) through the halo. To convert to the measured count rate $d^2N/dE_\gamma dt$, we evaluate $\mathcal{I}_{DM}$ for the 0-bounce and 2-bounce apertures, and fold $\mathcal{I}_{DM}$ with the appropriate solid angles, effective areas, and detector response matrices.

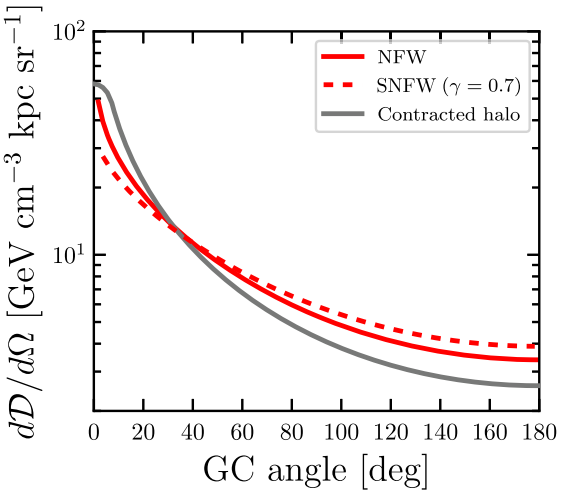

FIG. 1. DM column density $d\mathcal{D}/d\Omega \equiv \int_{LOS}\rho_\chi ds$ versus angle from the GC for NFW and SNFW profiles, as well as the contracted halo of Ref. [51]. Most NuSTAR observations in this work are at moderate distances from the GC, minimizing profile uncertainties. See Sec. II D for further details.

The choice of DM density profile ρ_χ as a function of galactocentric distance r is an important consideration for indirect DM searches. One popular choice of profile is the generalized Navarro-Frenk-White profile $\rho_{GNFW} \propto (r/r_s)^{-\gamma}[1 + (r/r_s)]^{\gamma-3}$, where r_s is the scale radius [44]. We consider a canonical DM-only NFW profile with $\gamma = 1$ [45] as well as a shallow (SNFW) profile with $\gamma = 0.7$ [46,47], with both NFW variants having local DM density $\rho_\chi(r_\odot) = 0.4$ GeV cm^{-3} [48–50]. Finally, we consider the contracted Milky Way halo model of Ref. [51] with local DM density $\rho_\chi(r_\odot) \approx 0.3$ GeV cm^{-3}, though since this model is only validated for $r > 1$ kpc, we conservatively assume that the DM density within $r < 1$ kpc is constant. For all Galactic DM profiles, we adopt $r_\odot = 8.1$ kpc for the Sun's galactocentric distance [52]. The DM column density as a function of viewing angle from the Galactic Center (GC) is shown in Fig. 1. So that we may set conservative upper limits on the DM decay rate, we do not include enhancements to the DM column density either from extragalactic sources or from possible substructure in the Milky Way (MW) halo. The impact of different profile choices on our DM decay limits is discussed in Secs. V B and V C.

III. NUSTAR SPATIAL GRADIENT ANALYSIS

In this section, we describe a novel application of the NuSTAR 0-bounce technique to dark-matter searches to

stacked ∼7-Ms/detector exposures of blank-sky fields: using the known spatial gradient of 0-bounce photons on the detectors to separate instrumental backgrounds from astrophysical x-ray emission.

A. NuSTAR observations and data processing

The NuSTAR dataset used in our spatial-gradient analysis was previously analyzed in a study of the cosmic x-ray background (CXB, Ref. [43]); here, we review several key aspects. The observations were conducted from 2012–2016 as part of the NuSTAR extragalactic survey program of the COSMOS [53], EGS [54], ECDFS [55], and UDS [56] blank-sky fields. Initial data reduction was performed with NUSTARDAS V1.8.0, with the flags `SAAMODE=strict` and `TENTACLE=yes` used to exclude NuSTAR passages through the South Atlantic Anomaly (SAA). A threshold of 0.17 counts s^{-1} in the 3–10 keV range on FPMA and FPMB was used as a threshold for excluding observations due to heightened solar and/or geomagnetic activity. Following these cuts, the total cleaned exposure time for the NuSTAR detectors is ∼7 Ms/FPM, shown in Fig. 2. We do not exclude any detector regions corresponding to known astrophysical x-ray sources, as these sources tend to be few in number and faint in comparison to the unresolved CXB; instead, we allow any faint sources in the FOV to contribute to the 0-bounce spectrum.

The average exposure time per detector versus angular distance from the GC is shown in Fig. 2 for both analyses described in this work. The extragalactic survey fields included in the present spatial-gradient analysis are located at similar distances from the GC (∼95–110°), and thus share similar DM column densities. Finally, the high latitudes of these fields ($|b| \sim 40$–$60°$) place them far from x-ray line or continuum emission in the Galactic plane.

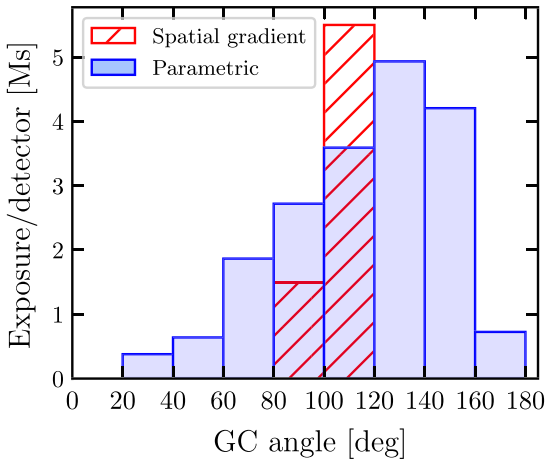

FIG. 2. Average cleaned exposure time per detector for the spatial-gradient analysis of Sec. III (red hatched) and the parametric analysis of Sec. IV (blue shaded) versus angular distance from the Galactic Center.

B. Spatial-gradient analysis

The crux of the spatial-gradient analysis is the fact that photons observed by NuSTAR have different spatial geometries when considered in detector coordinates. First, internal detector backgrounds (both line and continuum) are observed to have an essentially uniform distribution across each detector, though the overall rates between detectors may differ as a result of their different thicknesses (further discussed in Sec. IV B). Second, the focused CXB component includes both 2-bounce photons from the $13' \times 13'$ focused FOV (whose detector gradient follows the vignetting of the optics) and 1-bounce "ghost-ray" photons up to 30′ off axis [57]. Finally, the 0-bounce photons hitting the detectors from ∼1–3° off axis (principally from the CXB) manifest as a "Pac-Man" shaped gradient on the detectors. The solid angle of sky observed by each pixel (and hence the intensity pattern on the detector, assuming a uniform flux across the 0-bounce FOV) can be readily calculated from the known positions of the NuSTAR detectors, aperture stops, and optics bench using the NUSKYBGD code [42].

From this, we constructed the same likelihood model as that used in Ref. [43], with two spectral components: a spatially uniform internal detector component, and a 0-bounce component following the "Pac-Man" spatial gradient. We divide the 3–20 keV energy range into 100 bins equally spaced in $\log_{10} E_\gamma$, and bin the data using the 64×64 RAW detector pixels (32×32 pixels per detector chip) to provide sufficient counts in each energy bin. The expected total counts $N_{\rm pix}$ accumulated in the ith pixel during exposure time T is given by

$$N_{{\rm pix},i}(E_\gamma) = (C_{\rm int} M_{\rm int} + C_{0b} R_{\rm pix} \mathcal{E}_{\rm tot} A\Omega)_i T, \qquad (2)$$

where $C_{{\rm int},i} \equiv (dN/dt)_i$ is the internal background event rate, $M_{\rm int}$ encodes the nonuniformity and differences in relative normalization between the eight detectors obtained using 10–20-keV occulted data, $C_{{0b},i} \equiv (dF/d\Omega)_i$ is the 0-bounce flux per solid angle, $\mathcal{E}_{\rm tot} \equiv \mathcal{E}_{\rm det}\mathcal{E}_{\rm Be}$ is the energy-dependent transmission coefficient of the inactive detector surface layer and beryllium entrance window as described in CALDB V20200813, $R_{\rm pix}$ is the matrix encoding the nonuniform pixel response in the NuSTAR CALDB, A_i is the physical $(0.6\ {\rm mm})^2$ area of each pixel, Ω_i is the effective 0-bounce solid angle calculated using NUSKYBGD, and T is the exposure time of the observation. We do not include a focused CXB component for several reasons. First, the focused CXB signal is expected to be faint—nearly an order of magnitude fainter than the 0-bounce CXB signal (see Fig. 9 of Ref. [42]). The focused CXB signal is thus at or below the level of the internal detector background, making it extremely challenging to detect the spatial variations in the focused CXB signal. Second, the spatial variations in the focused CXB signal are further flattened when the data are binned in RAW detector pixels.

Thus, our analysis does not distinguish the focused CXB signal from the spatially flat internal detector background, so we allow the former component to be absorbed by the latter.

For each energy bin, we construct the likelihood (suppressing the E_γ dependence for clarity)

$$\mathcal{L} = \prod_i \left[\frac{N_{\rm pix}^{\mathcal{N}} \exp[-N_{\rm pix}]}{\mathcal{N}!}\right]_i \tag{3}$$

and minimize $-2\ln\mathcal{L}$ with respect to $C_{\rm int}$ and $C_{\rm 0b}$, where $\mathcal{N}_i$ is the observed number of counts in the ith pixel. The product runs over all pixels and NuSTAR observations. This produces nearly pure 0-bounce spectra and their corresponding detector response files for both FPMs. Modulo the narrower energy bins in this work, the spectra of Ref. [43] are identical to those shown here.

(We note that this data processing was completed before the release of the updated CALDB V20211020, which modified the 2-bounce vignetting profile, detector response matrices, and inactive CdZnTe throughput $\mathcal{E}_{\rm det}$. Of these, changes in $\mathcal{E}_{\rm det}$ have the greatest effect on our DM constraints; however, the variations in $\mathcal{E}_{\rm det}$ between CALDB versions are $\sim$5% at $E_\gamma = 3$ keV, with the agreement improving with increasing E_γ. In any case, this effect is subdominant compared to the $\sim$15–25% DM profile uncertainties discussed in Sec. V B.)

C. Spectral model

To fit the resulting unfolded spectra for FPMA and FPMB, shown in Fig. 3, we construct the model from Ref. [43] in XSPEC 12.11.1. The CXB intensity $\mathcal{I}_{\rm CXB} \equiv d^2F_\gamma/dE_\gamma d\Omega$ is parametrized by the model proposed by Ref. [58] for the energy range 3–60 keV, rescaled from units of $\rm sr^{-1}$ to $\rm deg^{-2}$ for convenience:

$$\mathcal{I}_{\rm CXB} = 0.0024\left(\frac{E_\gamma}{1\ \rm keV}\right)^{-\Gamma_{\rm CXB}} \times \exp\left[-\frac{E_\gamma}{E_{\rm fold}}\right]\ \rm cm^{-2}\,s^{-1}\,deg^{-2}\,keV^{-1}. \tag{4}$$

We adopt the canonical values $\Gamma_{\rm CXB} = 1.29$ and $E_{\rm fold} = 41.13$ keV proposed in Ref. [58] and shown to provide good fit quality in Ref. [43]. We also include an additional power-law model of the form $E_\gamma^{-\Gamma_{\rm solar}}$ to account for any residual solar emission particularly during the active years $\sim$2013–2014, with both the overall flux level and spectral index of the solar component allowed to vary (though we impose a limit $\Gamma_{\rm solar} > 2$ to prevent the solar component from becoming degenerate with the CXB). We do not include a model component to account for x-ray attenuation in the interstellar medium (ISM), as the equivalent neutral hydrogen column density $N_{\rm H}$ in the direction of these high-latitude survey fields is small, $\lesssim 2\times10^{20}\ \rm cm^{-2}$ [59,60]. (Adopting the attenuation cross sections from Ref. [61] and solar elemental abundances from Ref. [62], this corresponds to an equivalent optical depth $\tau \sim 10^{-3}$ at 3 keV, indicating negligible ISM attenuation that further decreases with energy).

With only three free parameters, we obtain good fits with $\chi^2/97 = 1.20$ for FPMA and 1.17 for FPMB

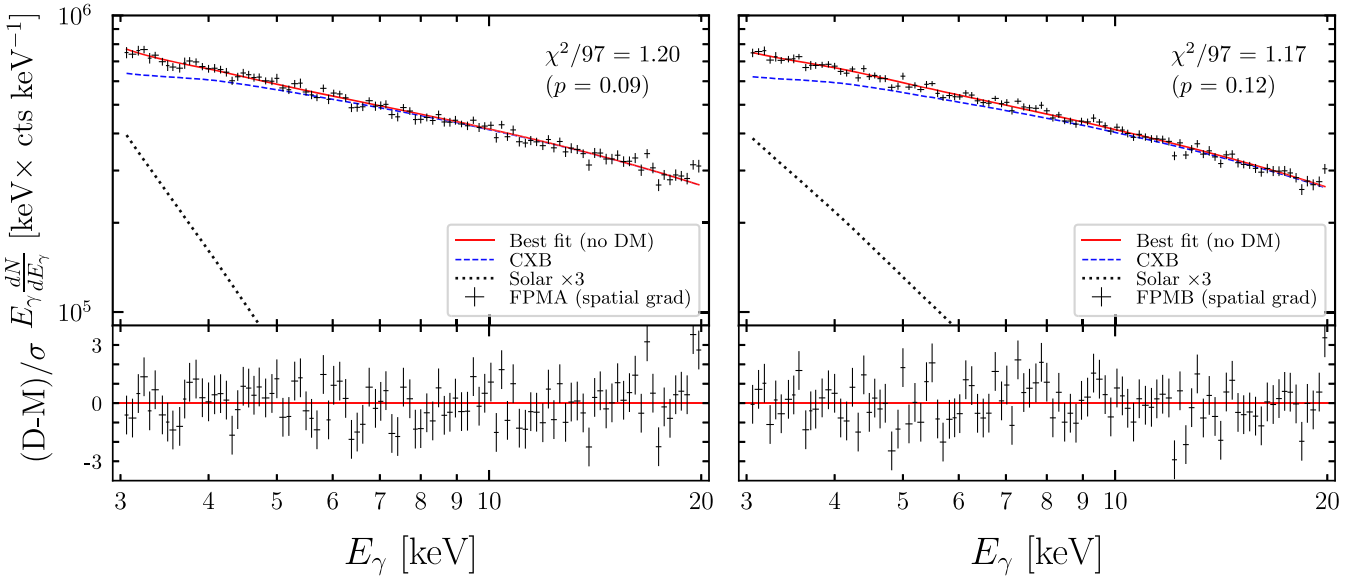

FIG. 3. 0-bounce spectra and best-fit models without DM, derived from the NuSTAR spatial-gradient technique for FPMA (left) and FPMB (right). The spectra $d^2F_\gamma/dE_\gamma d\Omega$ are scaled by the nominal exposure time (7 Ms), effective area (12.5 $\rm cm^2$) and solid angle (4.5 $\rm deg^2$) for presentation. The solar power-law normalization is multiplied by a factor of three for visibility. The bottom panels show the residuals (data minus model) scaled by statistical uncertainty σ.

TABLE I. Best-fit parameters and 68% confidence intervals for the CXB and solar power law for the NuSTAR spectra derived from the spatial-gradient analysis. The energy fluxes $\mathcal{F}^{\rm CXB}_{\rm 3–20\ keV}$ and $\mathcal{F}^{\rm solar}_{\rm 3–20\ keV}$ have units 10^{-11} erg cm^{-2} s^{-1} deg^{-2}.

Module	$\mathcal{F}^{\rm CXB}_{\rm 3–20\ keV}$	$\mathcal{F}^{\rm solar}_{\rm 3–20\ keV}$	$\Gamma_{\rm solar}$
FPMA	$2.82^{+0.02}_{-0.02}$	$0.07^{+0.01}_{-0.01}$	$4.5^{+0.5}_{-0.4}$
FPMB	$2.77^{+0.03}_{-0.04}$	$0.13^{+0.03}_{-0.02}$	$3.3^{+0.4}_{-0.4}$

(p-values 0.09 and 0.12, respectively). The best-fit energy fluxes $\mathcal{F}_{\rm 3–20\ keV} \equiv \int_3^{20} E_\gamma \mathcal{I}\, dE_\gamma$ and solar power-law indices are given in Table I. The CXB fluxes for FPMA and FPMB agree with each other and with the results of Ref. [43] at the few percent level, consistent with the expected cross calibration uncertainty between the FPMs. To ensure that our eventual DM limits are consistent with the expected statistical fluctuations, we simulate 10^3 spectra each for FPMA and FPMB using the XSPEC tool FAKEIT by convolving the best-fit models in Table I with the appropriate instrument response files and injecting Poisson noise. These mock spectra are then passed through the same analysis chain as the original spectral data in Sec. V.

IV. NUSTAR PARAMETRIC BACKGROUND ANALYSIS

In this section, we describe the development of an improved parametrization of the NuSTAR instrument background, and its application to ∼20-Ms/detector stacked exposures spread across the sky.

A. NuSTAR data processing

We considered all observations from 2012–2017, minus those from Sec. III to produce a dataset independent from the spatial-gradient analysis, leaving ∼2000 observations with exposure > 1 ks. Our data processing strategy was optimized to provide as "clean" a spectrum as possible (i.e., minimizing contamination from astrophysical sources and geomagnetic/solar activity) while accumulating as much observation time as possible. To prevent contamination from diffuse emission and point sources in the Galactic plane, we conservatively exclude all observations with Galactic latitudes $|b| < 15°$. This leaves ∼600 observations to analyze, listed in [63].

We begin the point-source removal process by creating a single 3–30 keV image per observation, smoothed with a Gaussian kernel of radius 6 pixels. Any candidate source with peak intensity greater than five times the expected background rate from NUSKYBGD is flagged and fit with a circular exclusion region. The radius of this region is determined by the peak intensity value in relation to a model point-spread function (PSF) as described in previous work [40]. To ensure the wings of the PSF have minimal influence on the resulting spectra, we define the outer boundary of the source exclusion regions such that the source event rate falls below 3% of the expected background rate. This creates exclusion regions many times the apparent size of the source, but due to NuSTAR's extended PSF, allows us to confidently utilize images with known sources.

At this stage, background light curves (excluding detected sources but still containing photons from faint 0-bounce and/or 2-bounce sources) would ideally have no temporal variation. However, SAA passages each orbit temporarily increase the detector background, particularly at energies $E_\gamma \gtrsim 50$ keV, and enhanced solar activity can increase the background at energies $E_\gamma \lesssim 10$ keV. These variations occur on generally short (few-minute) timescales compared to the ∼day-length timescales of individual NuSTAR observations. As such, these "flaring" periods can be readily identified as deviations from the mean background rate and removed; however, some light curves even without flaring exhibit an overall sinusoidal variation with a period ∼1 day, resulting from precession of the observatory's orbital motion with respect to the geomagnetic rigidity cutoff [64]. This sinusoidal variation must be accounted for to ensure proper identification and removal of flaring events.

To minimize bias in the initial processing, we implement a data-driven procedure to exclude flares. Following astrophysical x-ray source exclusion, we filter the event files to include only the energy range 50–100 keV. This energy band contains many fluorescence and activation features of the NuSTAR instrument, which are particularly sensitive to flaring. We exclude all time intervals whose event rate is $> 3.5\sigma$ above the expected background rate, with a second filtering step performed to exclude any low-level flares missed due to the presence of a larger flare. Finally, a source exclusion region, if it exists, is then applied to the 3–7 keV energy band where the Sun is the dominant contribution to the event rate, but still below the event rate expected from astrophysical x-ray sources. The average exposure time per detector as a function of angle from the Galactic Center is shown in Fig. 2.

At this stage, the event files have been filtered both spatially (removing astrophysical x-ray sources and creating separate event files for each detector) and temporally (removing flaring periods). From these filtered event files, we extract spectra and 2-bounce effective area curves $A_{\rm 2b}(E_\gamma)$ from each detector individually using NUSTARDAS V2.0.0 and calibration database (CALDB) V20200813 in extended-source mode. The $A_{\rm 2b}$ curves incorporate the beryllium shield throughput $\mathcal{E}_{\rm Be}$ but not the detector dead layer throughput $\mathcal{E}_{\rm det}$, as the latter is applied later. We use NUSKYBGD to calculate the 0-bounce effective area $A_{\rm 0b}$ and solid angle $\Delta\Omega_{\rm 0b}$ for each cleaned single-detector event file. We create one stacked spectrum per detector with exposure times shown in Table II. The effective areas and solid angles for each stacked spectrum are the exposure-time-weighted averages of the individual observations. Note that $A_{\rm 0b}$ strictly

TABLE II. NuSTAR detector exposures and grasps for the parametric analysis described in Sec. IV. The average A_{0b} and $\Delta\Omega_{0b}$ are the exposure-time-weighted averages over the individual telescope pointings calculated using NUSKYBGD. The values in parentheses correspond to observations with no astrophysical source regions masked.

Detector	Exposure (Ms)	Avg. A_{0b} (cm^2)	Avg. $\Delta\Omega_{0b}$ (deg^2)
A0	18.8	1.22 (3.18)	2.20 (2.31)
A1	19.9	2.07 (3.14)	2.95 (2.82)
A2	20.0	2.57 (3.17)	6.75 (6.63)
A3	19.6	2.00 (3.13)	6.62 (6.32)
B0	18.9	1.24 (3.18)	7.22 (6.98)
B1	19.5	2.27 (3.15)	4.62 (4.63)
B2	19.8	2.57 (3.19)	1.14 (1.28)
B3	19.9	1.76 (3.12)	5.47 (5.41)

decreases after masking astrophysical source regions, with the greatest reductions occurring on detectors A0 and B0. This is a result of the optical axis landing on detectors A0 and B0, so images of targeted point sources—and hence their exclusion regions—land mainly on those detectors as well (and to a lesser extent on A3 and B3; see Fig. 5 of Ref. [33]). In contrast, $\Delta\Omega_{0b}$ may either increase or decrease following region masking, depending on blocking of the pixels by the optics bench (see Fig. 2 of Ref. [43]).

B. NuSTAR background model

The NuSTAR instrument background consists of four spectral components (CXB, internal continuum, internal lines, and solar, as shown in Table III) that vary with energy and position on the detector plane. Here, we describe the procedure used to derive a phenomenological model of the instrument background applicable to the ∼20-Ms/detector stacked spectra of Sec. IV A, as well as verifying the stability of the model from 2012–2017. We note at the outset that the model described in this section was derived for analysis of this specific dataset and its filtering/instrument background conditions, and may not be applicable to other observations and/or time periods. A full accounting of the updated NuSTAR background model will be the subject of upcoming work.

We begin by applying the original NuSTAR background model of Ref. [42] to stacked data taken while NuSTAR's FOV was both occulted by the Earth (OCC, determined by the elevation angle ELV between the telescope boresight and Earth's limb) and shaded from the Sun (NOSUN, determined by an onboard sensor), during which the event rate was dominated by the internal detector background. (NUSTARDAS defines the OCC mode to begin when ELV $< 3°$; however, we find that this is not sufficient to fully suppress x-rays from the brightest sources near the limb of the Earth, so we require ELV $< 0°$.) After this filtering, the stacked OCC-mode spectra had exposures ∼17 Ms/detector, further reduced to ∼4.5 Ms/detector when the NOSUN filter was applied. (To ensure the Sun remains well below the horizon during NOSUN periods, we also exclude data 300 seconds before and after each period of solar illumination.) Principal component analysis showed no significant spatial variation in the internal background across the detectors. The internal detector background can be divided into two components: a featureless continuum and a large set of lines. The internal continuum model is the same as Ref. [42], i.e., a broken power-law with $E_{\rm break} = 121.86$ keV and spectral indices $\Gamma_1 = -0.047$ and $\Gamma_2 = -0.838$ for energies below and above $E_{\rm break}$, respectively. (As before, we define the power law as $E_\gamma^{-\Gamma}$, i.e., the internal continuum increases with E_γ.) The internal continuum dominates the background for energies $E_\gamma \gtrsim 100$ keV and is taken to have the same shape (though potentially different normalizations) for each detector.

The internal detector background lines deserve special consideration, as narrow lines can mimic a DM signal. We begin by applying the list of Lorentzian lines (plus internal continuum) from Ref. [42] to the data taken when the telescope's FOV was both occulted by the Earth and shielded from the Sun (OCC ∩ NOSUN). Inspection of the residuals showed the need for additional wide lines to model the "plateau" observed in the continuum for energies ∼10–20 keV. These features may result from the CXB-induced Earth x-ray albedo [65], though further study is ongoing. To check for any drift in the line positions and/or widths over time, we further divide each detector's 2012–2017 OCC ∩ NOSUN data into eight sequential

TABLE III. Summary of XSPEC model components for the parametric background analysis of Sec. IV. The detector RMFs and $\mathcal{E}_{\rm det}$ are taken from CALDB V20211020.

Component	XSPEC model	Response	Free parameters
CXB (0b)	`tbabs*powerlaw*highecut`	Detector RMF, $\mathcal{E}_{\rm Be}$, $\mathcal{E}_{\rm det}$, $\langle A_{0b}\Delta\Omega_{0b}\rangle$	None
CXB (2b)	`tbabs*powerlaw*highecut`	Detector RMF, $\mathcal{E}_{\rm Be}$, $\mathcal{E}_{\rm det}$, $\langle A_{2b}\Delta\Omega_{2b}\rangle$	0-bounce flux ±10%
Internal continuum	`bknpower`	Diagonal RMF	Normalization
Internal lines	$\sum$ `lorentz`	Detector RMF	Normalizations
Solar	`powerlaw` + $\sum$ `lorentz`	Detector RMF, $\mathcal{E}_{\rm Be}$, $\mathcal{E}_{\rm det}$	Powerlaw and line norms
DM line (0b)	`tbabs*gaussian`	Detector RMF, $\mathcal{E}_{\rm Be}$, $\mathcal{E}_{\rm det}$, $\langle A_{0b}\Delta\Omega_{0b}\rangle$	See Sec. V C
DM line (2b)	`tbabs*gaussian`	Detector RMF, $\mathcal{E}_{\rm Be}$, $\mathcal{E}_{\rm det}$, $\langle A_{2b}\Delta\Omega_{2b}\rangle$	See Sec. V C

periods of similar exposure time based on the observation date. As the detector chips share the same geometry and radiation environment, we expect their internal backgrounds to be highly correlated. Thus, we fit each stack's spectrum to the same internal continuum plus lines model described above. To account for uncorrelated variations between the chips (e.g., from unmodeled variations in detector gain), we also allow the line positions and widths to vary about their nominal positions. The line positions and widths for the final model of each detector (shown in Table IV) are then fixed to the weighted average of the best-fit values from each temporal stack. During our analysis, we allow the normalizations of the background lines to vary unless otherwise noted, to account for solar modulation, geomagnetic activity, and detector aging effects.

With a working model of the internal background for each detector, we next consider the full OCC-mode spectra, including both SUN and NOSUN periods. A component following the 0-bounce spatial gradient is clearly visible in detector images at low energies $E_\gamma \lesssim 10$ keV, indicating that solar x-rays (likely reflected from the mast and optics bench) are striking the detectors. Furthermore, the intensity of this component appears to be correlated to solar activity. This "solar" component includes both direct and reflected solar x-rays, and features a steeply falling continuum and several narrow lines. We model the continuum as a simple power-law to approximate the high-energy tail of a thermal plasma with temperature ∼few million K [66–69]. We attribute the lines to a combination of direct solar illumination and fluorescence from the telescope structural elements. Similarly to the treatment of the internal detector lines, we divide the full OCC-mode spectra for each detector into eight temporal slices, calculate best-fit solar spectral indices and line positions/widths for each, and average the values from each epoch to obtain the values in Table IV. This solar model is more flexible than the `apec` model of Ref. [42], as decoupling the continuum shape and line fluxes allows us to better model the solar background over a large fraction of the solar activity cycle. We caution that the solar power-law and line parameters were derived with the specific filtering conditions used in this analysis, and will likely vary considerably (and unpredictably) with different solar cycle conditions.

Finally, we consider the CXB, which is the dominant astrophysical background once bright sources have been removed. As discussed previously, there are simultaneous 0-bounce and 2-bounce CXB contributions with the same underlying sky intensity $\mathcal{I}_{\rm CXB} \equiv d^2F_\gamma/dE_\gamma d\Omega$. The 2-bounce CXB is modulated by energy-dependent effective area $A_{\rm 2b}(E_\gamma)$ of the optics, whereas the 0-bounce CXB is modulated only by the geometry of the aperture stops, optics bench, and detectors. (Both CXB components are modulated by the Be window and detector dead-layer throughputs $\mathcal{E}_{\rm Be}$ and $\mathcal{E}_{\rm det}$.) We adopt the same CXB model as Sec. III C, though here we also include an interstellar medium absorption component via the XSPEC model TBABS with equivalent hydrogen column $N_{\rm H} = 4.7 \times 10^{20}$ cm^{-2} (averaging over all observations) and solar elemental abundances [59–62]. (Even at the lowest energy $E_\gamma = 3$ keV, the equivalent optical depth τ is still $\lesssim$ few $\times 10^{-3}$. Though the expected attenuation is $\lesssim 0.5\%$, we include it for completeness.) As the CXB spectral model and 0-bounce instrument response are well constrained at the ∼percent level [43], we completely freeze the 0-bounce CXB component; however, we allow the 2-bounce CXB normalization a nominal ±10% range to account for residual uncertainties in the 2-bounce effective area and solid angle following point-source removal.

C. Spectral fitting

As the backgrounds for each of the eight NuSTAR detectors are slightly different, we individually fit each chip's cleaned on-sky science-mode spectrum (to be contrasted with the Earth-occulted OCC spectra) to the model described in Sec. IV B and Table IV. For all model components except the internal continuum (whose energy response is purely diagonal), we use the V3 redistribution matrix files (RMFs) from CALDB V20211020 [41]. All model components except the internal continuum and internal lines also include the Be window and CdZnTe dead-layer transmission efficiencies $\mathcal{E}_{\rm Be}$ and $\mathcal{E}_{\rm det}$, also taken from CALDB V20211020. For the 0-bounce CXB, we use the effective areas $A_{\rm 0b}$ and solid angles $\Delta\Omega_{\rm 0b}$ from Table II. For the 2-bounce CXB, we construct FOV-averaged $\langle A_{\rm 2b}\Delta\Omega_{\rm 2b}\rangle$ for each detector by averaging the effective areas and solid angles from the individual observations (see Sec. IV A). The $A_{\rm 2b}$ were calculated before the updated CALDB V20211020 became available, though as described in Sec. IV B we allow the 2-bounce CXB component to vary in overall normalization by ±10% to account for residual uncertainties in the effective area. In any case, the impact on our DM constraints is expected to be marginal compared to the ∼20% DM profile uncertainties.

With ∼20 Ms exposure per spectrum, even with the finest possible binning (one bin per 40-eV NuSTAR channel), the statistical uncertainty is at the level of a few percent per bin. The small statistical uncertainties allow systematic deviations—especially in the vicinity of background lines—to become visible. This is expected, as the line centroids and FWHMs are known to drift over the years. We address these systematics in two ways. First, we assign a flat 2.5% systematic uncertainty added in quadrature to the statistical uncertainty in each bin, sufficient to give $\chi^2/{\rm dof} \sim 1$. Second, as discussed in Sec. V C, we power constrain our DM limits to mitigate the effects of downward fluctuations of data with respect to the model.

Owing to the complexity of the full parametric background model, it was not computationally feasible to simulate and model the many mock datasets needed for sensitivity estimates. Instead, we constructed one "Asimov"

dataset [70] per science-mode spectrum, in which the event rates per energy bin were set equal to their best-fit values (including the 2.5% systematic) using the models described in Secs. IV B and IV C. These Asimov spectra were passed through the same modeling and DM-search procedure as the real data.

V. NUSTAR DM SEARCH

With the background models described in Secs. III C and IV B we search our spectra for evidence of DM decay lines using the same general procedure as our previous NuSTAR analyses [36–38], which we summarize below.

A. Statistical formalism

For each trial DM mass m_χ in a given spectrum, we search for evidence of DM using the profile likelihood ratio [70,71]. We take the likelihood $\mathcal{L}$ to be a function of the count rate $\boldsymbol{y}$, the DM signal strength μ (here, the decay rate Γ), and the background model parameters $\boldsymbol{\eta}$. The test statistic (TS) in favor of the DM hypothesis is given by

$$\mathrm{TS}(\hat{\mu}|m_\chi) = -2\,\ln\left[\frac{\max_{\mu,\boldsymbol{\eta}}\mathcal{L}(\boldsymbol{y}|\boldsymbol{\eta},\mu)}{\max_{\boldsymbol{\eta}}\mathcal{L}(\boldsymbol{y}|\boldsymbol{\eta},\mu=0)}\right], \tag{5}$$

where $\hat{\mu} \geq 0$ is the best-fit positive signal strength. We also define an analogous quantity q used for obtaining an upper limit on the decay rate:

$$q(\mu|m_\chi) = -2\,\ln\left[\frac{\max_{\boldsymbol{\eta}}\mathcal{L}(\boldsymbol{y}|\boldsymbol{\eta},\mu)}{\max_{\mu,\boldsymbol{\eta}}\mathcal{L}(\boldsymbol{y}|\boldsymbol{\eta},\mu)}\right]. \tag{6}$$

For each trial mass m_χ, we scan through a range of signal strengths $\mu > 0$, allowing the background model parameters $\boldsymbol{\eta}$ to find their best-fit values. In particular, by allowing the DM line to assume the full strength of any background lines, we obtain conservative limits on the DM flux in the vicinity of these lines. In the large-count limit, the log-likelihood ratio (and hence TS and q) reduces to $\Delta\chi^2$ for a single degree of freedom:

$$\begin{cases} \mathrm{TS}(\hat{\mu}|m_\chi) \simeq \min_\mu[\chi^2(\mu|m_\chi)] - \chi^2(\mu=0|m_\chi) \\ q(\mu|m_\chi) \simeq \chi^2(\mu|m_\chi) - \chi^2(\hat{\mu}|m_\chi). \end{cases} \tag{7}$$

The detection significance in Gaussian standard deviations for a DM line in a single spectrum is thus simply $\sqrt{\mathrm{TS}}$. In the absence of detections above the 5σ threshold, we set one-sided 95% upper limits to be the signal strength μ_{95} where $q(\mu_{95}|m_\chi) = 2.71$). For the Asimov datasets described in Sec. IV C, the $\pm N\sigma$ containment bands around the median expected 95% upper limit occur where q increases from its minimum by $(1.64 \pm N)^2$ [70,72]. To incorporate constraints from multiple spectra k, we consider the object $\mathfrak{X}^2(\mu|m_\chi) = \sum_k \chi_k^2(\mu|m_\chi)$. The corresponding expressions for $\mathrm{TS}_{\mathrm{joint}}$ and q_{joint} are

$$\begin{cases} \mathrm{TS}_{\mathrm{joint}}(\hat{\mu}_{\mathrm{joint}}|m_\chi) = \min_\mu[\mathfrak{X}^2(\mu|m_\chi)] - \mathfrak{X}^2(0|m_\chi) \\ q_{\mathrm{joint}}(\mu|m_\chi) = \mathfrak{X}^2(\mu|m_\chi) - \mathfrak{X}^2(\hat{\mu}_{\mathrm{joint}}|m_\chi) \end{cases}, \tag{8}$$

where $\hat{\mu}_{\mathrm{joint}}$ is the joint maximum-likelihood signal strength considering all spectra (i.e., the minimum of $\mathfrak{X}^2$). We use Eq. (1) to convert the limits on $dF_{\mathrm{DM}}/d\Omega$ to limits on the decay rate Γ, where the effective DM column density $\overline{\langle d\mathcal{D}/d\Omega\rangle}$ is obtained by averaging over both the FOV and the fractional exposure time $\Delta t_k/T$ of each observation:

$$\overline{\left\langle\frac{d\mathcal{D}}{d\Omega}\right\rangle} = \sum_k\left[\frac{\Delta t}{T\Delta\Omega}\int_{\mathrm{FOV}}\xi\mathrm{d}\Omega\int_{\mathrm{LOS}}\rho_\chi ds\right]_k. \tag{9}$$

B. Constraints from spatial-gradient analysis

To the spectral models for FPMA and FPMB described in Sec. III C we add a DM line convolved with the 0-bounce instrument response. We scan 200 DM masses uniformly spaced in $\log_{10} m_\chi$ between 6–40 keV for both the data and 10^3 mock spectra (i.e., oversampling with respect to the detector energy resolution). The FPMA and FPMB spectra are scanned separately and the joint statistics are calculated as described previously. The obtained limits from both FPMA and B and their combination are in excellent agreement both with our simulations and the asymptotic expectations. Aside from an upward fluctuation in the detection significance for masses ∼38–40 keV, resulting from a few upward-fluctuating bins in each spectrum, we find no evidence of x-ray lines, demonstrating the power of the spatial-gradient technique for suppressing detector backgrounds. We note that a DM interpretation for the aforementioned excess is inconsistent with previous NuSTAR constraints [35–38]. Unlike the parametric limits described in Sec. V C, we do not power constrain the spatial-gradient limits, as we are able to generate both $\pm1\sigma$ and $\pm2\sigma$ containment bands by bootstrapping from our 10^3 simulated spectra.

The dominant systematic uncertainty on the spatial-gradient limits arises from the choice of DM profile. The NFW profile gives a column density $\overline{\langle d\mathcal{D}/d\Omega\rangle} \approx 5\ \mathrm{GeV\,cm^{-3}\,kpc\,sr^{-1}}$ at the position of these observations (∼100° from the Galactic Center) with the SNFW profile giving a column density ∼15% higher. On the other hand, the profile proposed by Ref. [51] gives a value ∼25% lower than our default NFW profile, a consequence of the contracted halo. Our spatial-gradient limits shown in Figs. 4 and 6 are derived using the NFW profile, which we take as a "median" column density.

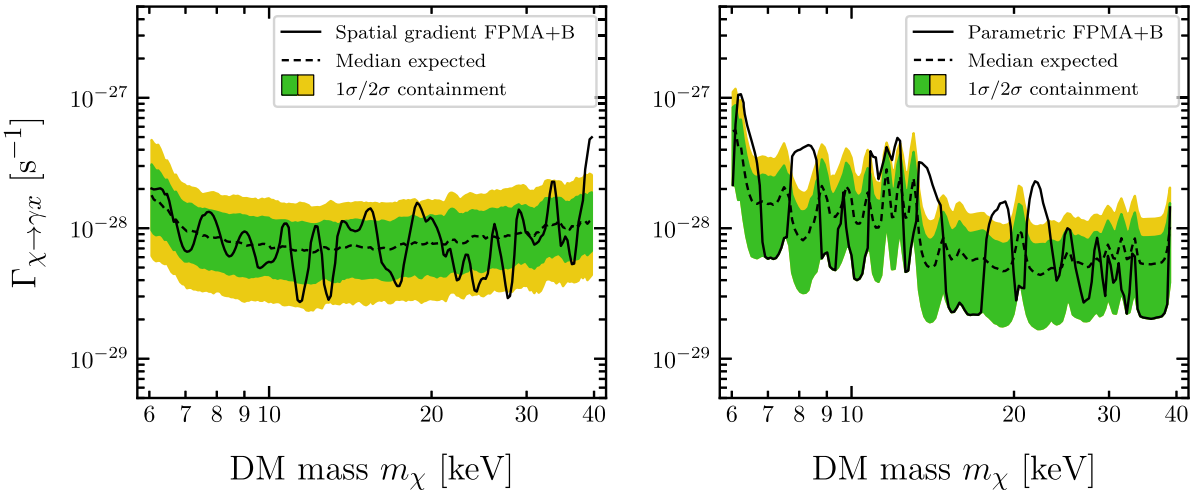

FIG. 4. Left: 95% confidence upper limits and expected containment on the single-photon decay rate $\Gamma_{\chi\to\gamma x}$ for the spatial-gradient method of Sec. III. Right: same quantity for the parametric method of Sec. IV. For two-photon decays $\chi\to\gamma\gamma$, e.g., for axionlike particles [73–76], the decay-rate limits in both plots are strengthened by a factor of 2. A comparison of all NuSTAR limits may be found in Fig. 5.

C. Constraints from parametric-modeling analysis

To search for evidence of decaying DM in the eight single-detector spectra (both data and Asimov mock spectra) of Sec. IV C, we adopt the same scanning strategy as described in Sec. V B, with two key differences. First, the background model is substantially more complex, a consequence of the many activation/fluorescence lines. As we are searching for anomalous x-ray lines in the energy range 3–20 keV, we freeze the normalizations of all lines between 20–95 keV to their best-fit values under the null-DM hypothesis. This procedure ensures that the minimizer does not become stuck in irrelevant local minima and greatly increases the scanning speed, with negligible impacts on our DM constraints compared to tests in which all lines are free to fit. Additionally, unlike the spatial-gradient case in which the 2-bounce contribution to the DM signal was negligible, here we model both the 0-bounce and 2-bounce contributions. Using the NFW profile, we find $\overline{\langle d\mathcal{D}/d\Omega\rangle}\approx 5$ GeV cm^{-3} kpc sr^{-1} for the 0-bounce and 2-bounce apertures, though this may vary in either direction by ∼20–25% if the SNFW or contracted profiles are considered. Scanning the eight individual-detector spectra k with a grid of 165 masses between 6–40 keV evenly spaced in $\log_{10} m_\chi$, we collect the distributions $q_k(\mu|m_\chi)$. (This is somewhat smaller than 200 mass bins in the spatial-gradient analysis of Sec. III, owing to the much greater complexity and computational cost of the full parametric model).

Similarly to Sec. V B, we calculate the line detection significance and one-sided 95% confidence upper limits for each of the eight spectra individually, as well as the joint constraints summing over all eight spectra. We identify five mass ranges in which the joint decay-rate limit significantly worsens compared to the expected values from the Asimov procedure: (i) ∼7.8–8.5 keV, (ii) ∼11–12 keV, (iii) ∼13–14 keV, (iv) ∼18–19 keV, and (v) ∼21–22 keV. In particular, the excesses in (i), (iii), and (v) have local significance $> 5\sigma$ and are observed on multiple detectors on both FPMs. We argue that none of these five excesses are consistent with decaying DM for several reasons. First, the spatial-gradient analysis finds no excesses with significance $> 2\sigma$ in these mass ranges, strongly constraining any astrophysical origin. Second, we note that all of these excesses occur near adjacent instrumental and/or solar lines, causing any mismodeling of these lines or the instrument response to be amplified. Finally, we observe that the excesses do not have consistent fluxes $dF/d\Omega$ across the detectors, contrary to the expectation of an approximately uniform intensity from decaying DM across the instrument FOV. [In particular, we note the strong excess at $E_\gamma\sim 4$ keV ($m_\chi\sim 8$ keV) on detector B2, despite this detector having a very small solid angle $\Delta\Omega_{0b}$].

In the absence of plausible DM detections, we instead set conservative upper limits on the decay rate, which would not exclude a DM signal with these decay rates if it were present. To avoid setting artificially strong limits as a result of downward fluctuations, and because the simple Asimov procedure we employed cannot be used to define the -2σ edge of the 95% confidence band, we power constrain our limits [77], i.e., the observed limit cannot run below the $(\text{median}-1\sigma)$ level expected from the Asimov simulations. These power-constrained limits are shown in Fig. 4.

D. Sterile-neutrino DM constraints

Specializing to the particular case of sterile-neutrino decays $\chi\to\gamma\nu$, we convert our limits on the model-independent single-photon decay rate $\Gamma_{\chi\to\gamma x}$ to

corresponding limits on the active-sterile mixing angle θ for Majorana neutrinos [78,79]:

$$\Gamma_{\chi\to\gamma\nu} = 1.38\times10^{-32}\ \mathrm{s}^{-1}\left[\frac{\sin^2(2\theta)}{10^{-10}}\right]\left(\frac{m_\chi}{1\ \mathrm{keV}}\right)^5. \quad (10)$$

Figure 6 shows the upper limits on the sterile-neutrino DM parameter space obtained in this work. For comparison, we also show previous limits from other x-ray searches from CXO [27], XMM-Newton [25,29], Suzaku [19], Fermi Gamma-ray Burst Monitor [22], and INTEGRAL Soft Photon Imager [12]. Our results further constrain the sterile-neutrino decay rate, especially for masses ∼15–18 keV and ∼25–40 keV, where the limit improves on previous NuSTAR constraints by a factor ∼2–3 and ∼5–10, respectively compared to previous NuSTAR constraints. We emphasize that these results are not specific to sterile-neutrino DM, but are also applicable to generic decaying DM models that involve a photon line, with the decay-rate limits given in Fig. 4.

With improved modeling in the low-energy NuSTAR background, our limits extend down to DM masses $m_\chi = 6$ keV, and have improved the limit by nearly an order of magnitude compared to previous NuSTAR results for masses below 10 keV [35,36]. Importantly, our results are now in tension with the claimed tentative signal at $E_\gamma \simeq 3.5$ keV [31,32]. Previous NuSTAR analyses included a line at 3.5 keV [35,36], attributed to instrument background due to its presence in Earth-occulted data, though a possible astrophysical contribution was debated. Our present results constrain the DM origin of the 3.5-keV line in complementary ways. First, the spatial-gradient analysis of Sec. III does not detect the 3.5-keV line. As the spatial-gradient technique suppresses detector backgrounds while remaining sensitive to astrophysical emission, its nonobservation simultaneously strongly constrains its astrophysical origin and favors its detector origin. Using the more traditional parametric modeling approach on a disjoint dataset covering a much larger area of the Galactic halo, we apply the improved model of the NuSTAR instrument background in Sec. IV B. In particular, this background model includes a ∼3.5-keV line detected in Earth-occulted data when no DM events are expected. The best-fit width of this line (∼0.5-keV FWHM prior to convolution with the detector response) is notably wider than the ∼0.4-keV FWHM detector resolution expected for an astrophysical line, suggesting it may be an artifact of variations in the detector dead-layer absorption or instrument response (which are rapidly varying at low energies) rather than a genuine spectral line. Whatever its origin, we are still able to set conservative constraints on a 3.5-keV astrophysical line by allowing the DM line in our search procedure to incorporate events from the internal background.

Modeling the spectra from each NuSTAR detector independently for the first time and combining the constraints, we obtain similar constraints to the spatial-gradient method across much of the 6–40 keV mass range, demonstrating the complementarity and consistency of the two approaches. Our null results on the 3.5 keV line obtained with standard statistical techniques are in agreement with recent results from CXO [27] and XMM-Newton [25,28,29] despite NuSTAR having a substantially lower effective area and shorter exposure time than either, illustrating the power of NuSTAR's wide FOV. (We note that the limits in Ref. [25] have led to much discussion in the literature [80–82].) Taken together, our results therefore provide strong and independent evidence against the astrophysical and DM interpretation of the 3.5-keV line in the Galactic halo.

In addition to the strong constraints at low masses, our present NuSTAR results are the strongest x-ray constraints on sterile-neutrino DM to date in the mass ranges ∼15–18 keV and ∼25–40 keV, improving on previous NuSTAR work by a factor ∼2–3 and ∼5–10, respectively (see Fig. 5). In particular, improvements in the parametric background model in the energy range ∼15–20 keV (mass range ∼30–40 keV) allow us to leverage the statistical power of the full ∼20-Ms dataset without being limited by modeling systematics as in previous works (see, e.g., Refs. [37,38]). These new results further demonstrate NuSTAR's ability to provide DM constraints in this challenging mass range, as the use of 0-bounce photons allows the observatory to sample large areas of the sky without being limited by the strong energy dependence of x-ray mirrors. Finally, we note that the NuSTAR limits in

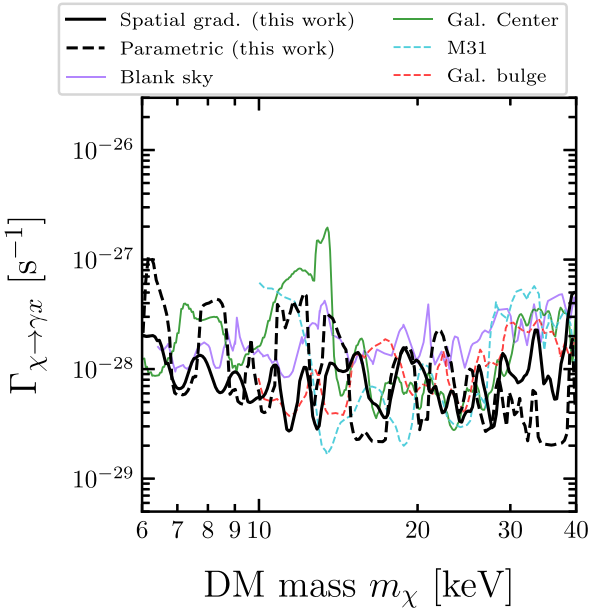

FIG. 5. Comparison of NuSTAR DM decay-rate limits from this work (black solid and dashed lines) and previous NuSTAR analyses of blank-sky extragalactic fields [83], the Galactic Center [36], M31 [37], and the Galactic bulge [38].

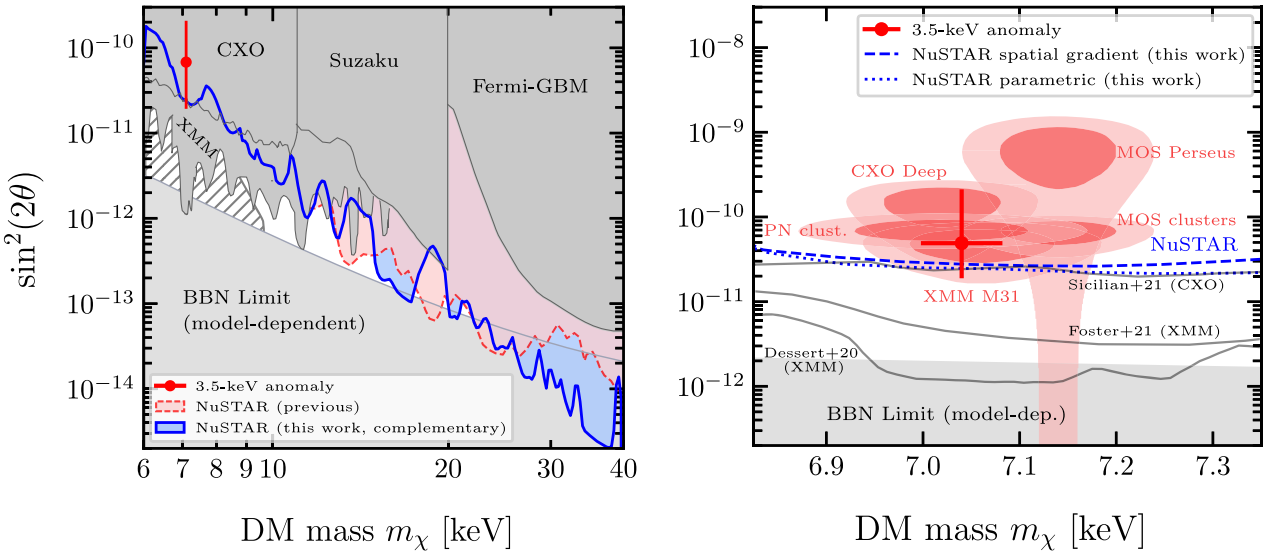

FIG. 6. Constraints on sterile-neutrino DM in the νMSM. Left: constraints on $\sin^2(2\theta)$ from previous NuSTAR analyses (light red shade and solid line, Refs. [35–38]) and other x-ray telescopes (dark gray, Refs. [19,22,25,27,29]) compared to the complementary NuSTAR constraints from this work (dark blue shade and solid line showing the parameter space excluded by either the spatial-gradient or parametric analysis, whichever is stronger at each mass) and an example of the 3.5-keV anomaly including DM profile uncertainties (red point, Ref. [32]). The gray hatched region represents structure-formation constraints from the observed number of MW dwarf satellites [88]. Right: enlarged version of the previous plot. The dark (light) red contours show the 1σ (2σ) detection regions of the 3.5-keV anomaly as detailed in Fig. 7 of Ref. [92]. The red cross representing the 3.5-keV anomaly is the same as the left-hand figure. Recent deep constraints from CXO (3σ upper limit, Ref. [27]) and XMM-Newton (95% upper limit, Refs. [25,29]) are compared to the NuSTAR constraints from this work (95% upper limit, blue dashed/dotted lines). See Sec. V D for further details.

this work are weaker than previous NuSTAR constraints from M31 [37] and the Galactic bulge [38] near $m_\chi \sim 14$ keV and $m_\chi \sim 19$ keV. At 14 keV, the FPMB spatial-gradient spectrum experiences a mild excess at $E_\gamma \sim 7$ keV, and the sensitivity of the parametric-modeling method is limited by a bright instrumental line at the same energy. At 19 keV, a similar weak excess is observed in the FPMB spatial-gradient spectrum, and the parametric model has difficulty reproducing the shape of the instrumental line at $E_\gamma \sim 10$ keV.

While our results are applicable to generic sterile-neutrino DM that mixes with SM neutrinos, they also have important implications for particular realizations of sterile-neutrino DM models. One popular scenario is sterile-neutrino DM produced by mixing with active neutrinos [8,9]. If more right-handed neutrinos are also present, e.g., in the νMSM [4,5,84,85], then it is also possible to explain baryogenesis and the origin of neutrino mass, solving three important problems in fundamental physics in the same framework.

Assuming that the DM is resonantly produced in the presence of a primordial lepton asymmetry [86], big bang nucleosynthesis (BBN) constraints on the lepton asymmetry [87] can therefore be used to set lower limits on the mixing angle θ, below which resonant production would underproduce DM compared to its observed abundance. In Fig. 6 we show the BBN constraints from STERILE-DM [86], adopting the lepton asymmetry per unit entropy density $L_6 \equiv 10^6(n_\nu - n_{\bar{\nu}})/s \leq 2500$. Additional discussion of these BBN limits may be found in, e.g., Refs. [7,38,88–91].

The velocity distribution of DM can suppress the formation of small-scale cosmological structure; thus, observational probes such as dwarf MW satellite galaxies [88,93,94] and the Lyman-α forest [95–98] can be used to placed limits on the "warmness" of sterile neutrino DM, thereby constraining sterile-neutrino mixing parameters. In Fig. 6, we show the MW satellite limit from Ref. [88] (consistent with that from [94]). We note, however, that these limits depend on both the sterile neutrino production physics [86,90] as well as the complex structure-formation processes needed to connect DM halos to the observed satellite galaxies. These structure-formation processes have substantial uncertainties, and stronger/weaker constraints (see, e.g., Refs. [99–101]) can be obtained with different models of galaxy formation [94]. Even if only the more conservative structure-formation limits of Ref. [88] are considered, it is clear that the combination of several types of constraints have nearly closed the window for keV-range sterile neutrino dark matter, and that new work is needed to ensure robust sensitivity across the entire range.

VI. CONCLUSIONS

In this work, we obtain updated limits on DM decaying into monoenergetic photons with the NuSTAR x-ray

observatory. We consider two complementary analyses conducted on disjoint datasets to leverage the full power of the available NuSTAR data: the spatial-gradient method, utilizing a novel geometric technique to greatly suppress the detector background; and a more traditional parametric method, combining a large amount of data with an updated model of the NuSTAR instrument background. Significantly, we are able to use the full NuSTAR energy range down to $E_\gamma = 3$ keV, allowing us to sensitively test lower-mass DM candidates. These analyses complement and extend previous NuSTAR DM searches in the Milky Way and the M31 galaxy, which have large amounts of DM [35–38].

Our new analyses provide significant DM constraints in two key mass ranges. First, our improved treatment of the low-energy instrument background allows us to strongly constrain a possible DM origin of the 3.5-keV anomaly using standard statistical techniques. Second, our constraints on DM masses ∼15–40 keV continue to fill in the sterile-neutrino parameter space down to—and below—the BBN limit. Our results are also applicable to other DM candidates decaying or annihilating into monoenergetic photons, e.g., axionlike particles [73–76]. If taking the latest results from satellite counting into account [94,100], the full parameter space is now mostly covered, which is an important milestone. While this does not fully rule out sterile neutrinos as the only DM component, it does show that the simple and elegant mixing production mechanism [8,9] may be insufficient, and more involved modeling [6,102–104] may be required to make sterile neutrinos a viable DM candidate. Ongoing and near-term missions such as Spektr-RG [105,106], Micro-X [107], and XRISM [108], and proposed missions such as Athena [109], AXIS [110], eXTP [111], HEX-P [112], and Lynx [113] are hoped to further constrain the sterile-neutrino parameter space using various detector architectures and observing strategies [83,114–118].

ACKNOWLEDGMENTS

We are grateful to the NuSTAR team for the excellent performance of the observatory and their assistance with data processing. We also thank Alexey Boyarsky, Josh Foster, Nick Rodd, Field Rogers, Mengjiao Xiao, and the anonymous reviewer for helpful comments and discussions. B. M. R. and K. P. thank Paul Acosta, Gabriel Collin, and the MIT Laboratory for Nuclear Science for computing support. B. M. R. and K. P. were supported by the Cottrell Scholar Award, Research Corporation for Science Advancement (RCSA), ID No. 25928. S. R. and D. R. W. were supported by NASA Grant No. 80NSSC18K0686. K. C. Y. N. was supported by the Research Grants Council (RGC) of HKSAR, Project No. 24302721. J. F. B. was supported by U.S. National Science Foundation (NSF) Grant No. PHY-2012955. B. W. G. was supported by NASA Contract No. NNG08FD60C. S. H. was supported by the U.S. Department of Energy Office of Science under Award No. DE-SC0020262, NSF Grants No. AST-1908960 and No. PHY-1914409, JSPS KAKENHI Grant No. JP22K03630, and the World Premier International Research Center Initiative (WPI Initiative), MEXT, Japan. R. K. was supported by Russian Science Foundation Grant No. 22-12-00271. This research has made use of data and/or software provided by the High Energy Astrophysics Science Archive Research Center (HEASARC), which is a service of the Astrophysics Science Division at NASA/GSFC.

APPENDIX A: PARAMETRIC BACKGROUND MODEL

In this section, we list the values of the parameters used to define the background model of Sec. IV. The values of these parameters are all frozen during our dark-matter analysis.

TABLE IV. Parameters for the background model of Sec. IV B. "Int. lines" and "Int. cont." refer to the internal detector lines and continuum, respectively. Line centroids E_0 and FWHM are given in keV. We provide two decimal places for the line E_0 and FWHM for numerical reasons, and are not indicative of precision.

		FPMA				FPMB			
Model	Parameter	Detector A0	Detector A1	Detector A2	Detector A3	Detector B0	Detector B1	Detector B2	Detector B3
Int. lines	E_0, FWHM	3.47, 0.76	3.53, 0.81	3.57, 0.82	3.50, 0.68	3.65, 0.84	3.62, 0.83	3.47, 0.67	3.43, 1.22
		4.44, 0.00	4.40, 0.05	4.38, 0.26	4.30, 0.22	4.86, 0.01	4.40, 0.00	4.46, 0.15	4.57, 0.14
		5.12, 1.43	5.16, 1.41	5.08, 1.21	5.01, 0.87	5.15, 1.37	5.17, 1.59	4.89, 0.00	4.89, 0.12
		6.20, 0.00	6.19, 0.02	6.12, 0.00	6.13, 0.00	6.19, 0.09	6.11, 0.14	6.50, 0.00	6.13, 0.00
		7.40, 0.00	7.39, 0.05	7.38, 0.12	7.34, 0.02	7.40, 0.00	7.42, 0.05	7.90, 0.00	7.43, 0.00
		7.90, 0.00	7.90, 0.00	7.90, 0.00	7.84, 0.00	7.90, 0.00	7.90, 0.00	8.05, 2.51	7.86, 2.78
		8.17, 3.30	8.15, 3.15	7.93, 2.89	7.88, 2.81	7.97, 3.06	8.20, 3.56	8.74, 0.00	7.88, 0.08
		8.66, 0.06	8.64, 0.00	8.64, 0.00	8.64, 0.01	8.75, 0.00	8.75, 0.10	9.14, 0.42	8.75, 0.17
		10.40, 0.58	10.24, 0.34	10.31, 0.37	10.19, 0.69	10.18, 0.50	10.29, 0.44	10.27, 0.73	10.26, 0.88
		11.40, 19.37	11.45, 16.85	11.04, 19.28	11.69, 19.37	11.63, 19.36	11.02, 18.34	10.79, 19.07	11.69, 0.00
		12.60, 0.00	12.60, 0.00	12.60, 0.00	12.60, 0.00	12.60, 0.00	12.60, 0.00	12.06, 0.00	12.60, 0.00
		13.20, 19.37	13.17, 0.77	13.17, 0.00	12.74, 18.47	13.20, 20.00	13.11, 20.00	13.17, 0.00	12.76, 19.37
		13.80, 19.37	13.20, 19.37	13.20, 19.37	13.17, 0.00	13.80, 20.00	13.17, 0.76	13.20, 19.37	13.23, 0.00
		14.20, 0.00	13.80, 19.37	13.80, 0.00	13.80, 0.00	14.20, 0.00	13.80, 0.00	13.93, 0.08	14.17, 1.13
		15.05, 0.38	14.99, 0.50	15.01, 0.27	14.84, 0.08	14.92, 0.00	14.71, 1.13	14.74, 0.73	14.83, 0.28
		16.00, 0.00	15.55, 0.05	15.95, 0.00	15.64, 0.00	15.73, 0.32	15.71, 0.09	15.72, 0.00	15.80, 0.00
		16.72, 0.10	16.63, 0.07	16.64, 0.00	16.47, 0.00	16.79, 0.00	16.64, 0.00	16.67, 0.06	16.79, 0.00
		19.56, 0.00	19.30, 0.10	19.55, 0.58	19.49, 0.58	19.60, 0.25	19.54, 0.05	19.52, 0.13	19.52, 0.01
		21.82, 0.63	21.81, 0.66	21.85, 0.98	21.81, 1.42	21.82, 0.59	21.75, 0.65	21.75, 0.68	21.75, 0.48
		22.86, 0.01	22.85, 0.06	22.89, 0.27	22.86, 0.57	22.92, 0.00	22.89, 0.11	22.89, 0.19	22.93, 0.18
		24.71, 1.65	24.74, 1.69	24.71, 1.52	24.66, 1.56	24.72, 1.82	24.76, 1.82	24.72, 1.70	24.83, 2.02
		25.23, 0.14	25.22, 0.16	25.23, 0.18	25.19, 0.18	25.23, 0.17	25.22, 0.15	25.23, 0.21	25.24, 0.20
		27.90, 1.21	27.92, 1.39	27.97, 0.00	27.97, 0.00	27.97, 1.47	27.92, 1.47	27.97, 1.48	27.93, 1.48
		28.08, 0.00	28.12, 0.00	28.02, 1.47	28.02, 1.72	28.13, 0.00	28.14, 0.00	28.43, 0.29	28.08, 0.00
		28.44, 0.20	28.44, 0.21	28.44, 0.31	28.44, 0.40	28.44, 0.21	28.44, 0.20	30.30, 0.55	28.45, 0.27
		30.31, 0.50	30.30, 0.55	30.27, 0.75	30.20, 0.82	30.30, 0.68	30.30, 0.57	30.78, 0.42	30.33, 0.52
		30.78, 0.37	30.77, 0.34	30.81, 0.51	30.81, 0.55	30.78, 0.34	30.77, 0.35	32.04, 0.66	30.79, 0.44
		32.07, 0.57	32.11, 0.49	32.02, 0.80	31.92, 0.90	32.13, 0.59	32.08, 0.46	34.88, 0.48	32.15, 0.48
		34.91, 0.53	34.89, 0.38	34.80, 0.75	34.87, 0.60	34.89, 0.54	34.89, 0.38	39.00, 8.03	34.95, 0.52
		38.55, 9.97	38.18, 8.89	38.76, 8.15	38.59, 7.00	39.17, 8.43	38.39, 8.85	39.31, 0.63	39.14, 9.89
		39.33, 0.49	39.30, 0.56	39.30, 0.78	39.21, 0.91	39.36, 0.44	39.35, 0.53	46.95, 9.97	39.40, 0.52
		47.39, 9.60	47.27, 8.67	47.58, 8.66	47.28, 8.26	47.15, 7.92	47.18, 8.45	47.03, 0.38	47.06, 9.49
		52.50, 1.19	52.46, 1.06	52.42, 1.35	52.28, 1.67	52.50, 1.12	52.49, 0.99	52.46, 1.07	52.55, 1.02
		57.83, 2.16	58.04, 3.02	57.96, 3.89	57.84, 3.65	57.59, 4.14	58.42, 3.45	57.94, 5.05	57.93, 4.74
		65.24, 7.95	65.28, 7.65	65.23, 6.51	65.38, 6.42	65.18, 7.31	64.88, 6.04	65.12, 5.91	65.20, 6.03
		66.93, 0.28	66.92, 0.34	66.98, 0.68	66.82, 0.87	67.00, 0.19	67.01, 0.56	67.01, 0.57	67.05, 0.44
		74.99, 2.83	75.42, 3.62	74.98, 3.68	75.14, 3.98	74.78, 2.84	75.28, 4.44	75.21, 4.31	75.30, 4.32
		76.75, 0.30	77.72, 3.26	77.72, 3.26	79.14, 3.91	76.72, 0.53	81.26, 0.27	82.36, 3.24	82.76, 3.12
		85.50, 8.06	85.87, 11.68	85.89, 4.82	86.66, 8.63	84.62, 7.19	85.45, 4.12	85.26, 2.25	85.04, 3.96
		87.83, 0.51	87.81, 0.38	87.77, 1.08	87.79, 0.78	87.83, 0.55	87.87, 0.52	87.84, 0.67	87.89, 0.63
		92.66, 0.36	92.71, 0.27	92.48, 0.95	92.76, 0.73	92.66, 0.36	92.71, 0.38	92.69, 0.51	92.72, 0.50
		105.36, 0.14	105.40, 0.67	105.19, 0.71	105.44, 1.54	105.35, 0.14	105.40, 0.02	105.35, 0.20	105.42, 0.06
		122.74, 1.22	127.27, 19.37	122.05, 1.39	125.46, 18.57	122.33, 1.11	122.41, 0.46	122.93, 2.12	122.25, 0.17
		144.57, 0.60	144.66, 0.80	144.26, 1.43	144.65, 1.55	144.59, 0.50	144.71, 0.16	144.56, 0.43	144.80, 0.24
Int. cont.	Γ_1	−0.047							
	Γ_2	−0.838							
	E_{break}	121.86 keV							

(Table continued)

TABLE IV. *(Continued)*

		FPMA				FPMB			
Model	Parameter	Detector A0	Detector A1	Detector A2	Detector A3	Detector B0	Detector B1	Detector B2	Detector B3
CXB	$N_{\rm H}$	4.7×10^{20} cm^{-2}							
	$\mathcal{F}^{\rm CXB}_{\rm 3-20\ keV}$	2.82×10^{-11} erg cm^{-2} s^{-1} deg^{-2}							
	$E_{\rm fold}$	41.13 keV							
	$\Gamma_{\rm CXB}$	1.29							
Solar	$\Gamma_{\rm sol}$	8.37	9.50	8.90	8.10	9.49	9.50	9.50	9.50
	E_0, FWHM	3.77, 0.00	3.77, 0.00	3.77, 0.00	3.77, 0.00	3.72, 0.00	3.72, 0.04	3.84, 0.00	3.77, 0.00
	E_0, FWHM	4.45, 0.48	4.46, 0.56	4.46, 0.56	4.46, 0.57	4.42, 0.32	4.46, 0.57	4.45, 0.55	4.40, 0.62
	E_0, FWHM	5.33, 0.63	5.33, 0.62	5.33, 0.62	5.33, 0.62	5.32, 0.74	5.33, 0.63	5.34, 0.62	5.35, 0.45
	E_0, FWHM	5.79, 0.00	5.80, 0.00	5.80, 0.00	5.80, 0.00	5.91, 0.00	5.80, 0.00	5.84, 0.00	5.80, 0.00
	E_0, FWHM	6.48, 0.22	6.48, 0.23	6.48, 0.23	6.48, 0.23	6.49, 0.13	6.48, 0.25	6.46, 0.35	6.47, 0.29

APPENDIX B: PARAMETRIC BACKGROUND ANALYSIS FITS

In this section, we show the best fits to the eight individual detector spectra (Figs. 7–14) using the parametric background model described in Sec. IV in the energy range 3–150 keV. As shown, the fit quality in

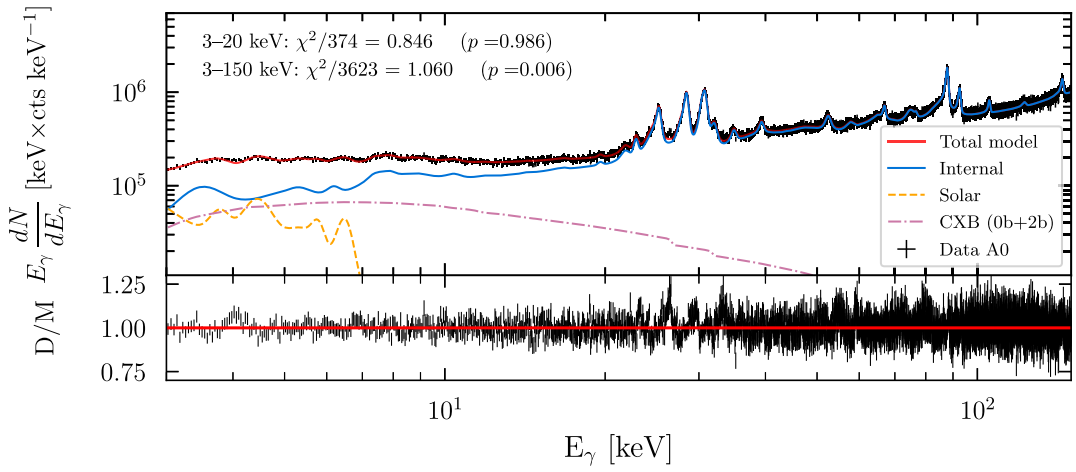

FIG. 7. Spectrum and best-fit parametric background model for detector A0 described in Sec. IV. The bottom panel shows the ratio data/model.

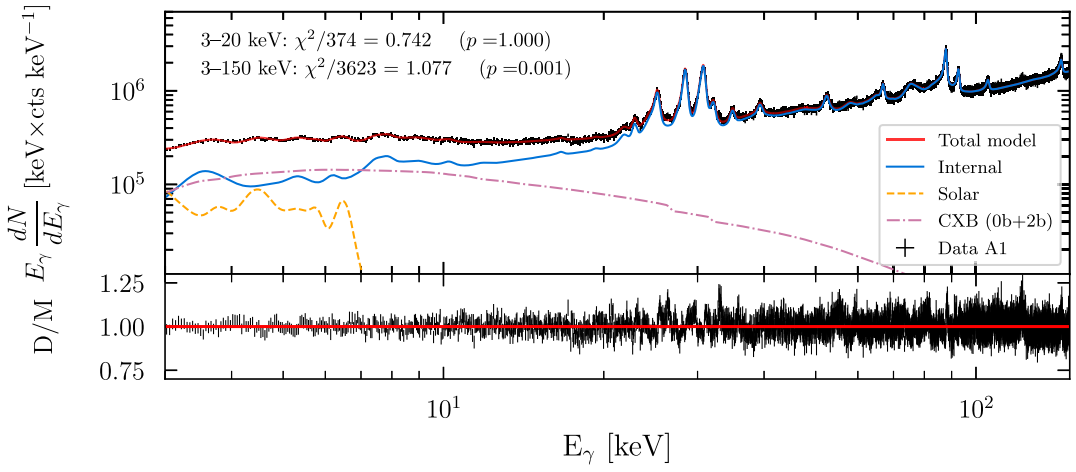

FIG. 8. Same as previous, for detector A1.

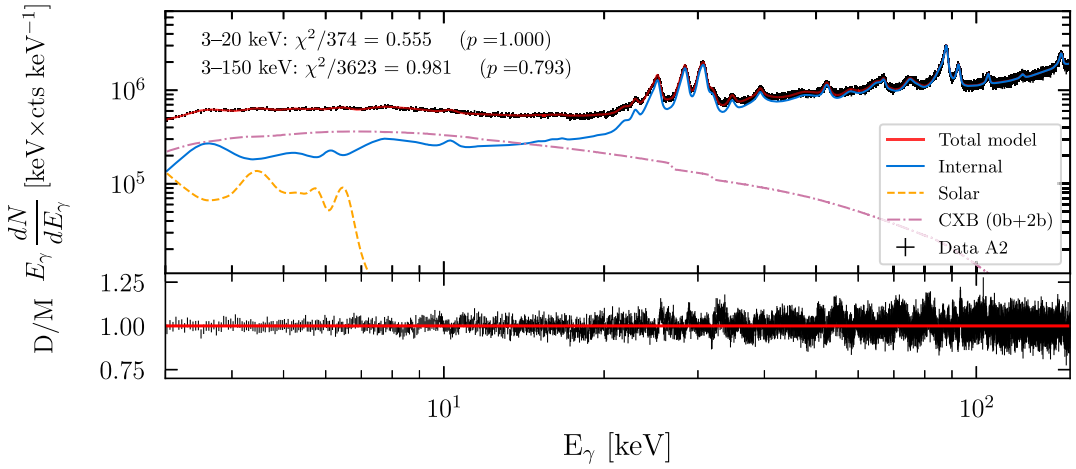

FIG. 9. Same as previous, for detector A2.

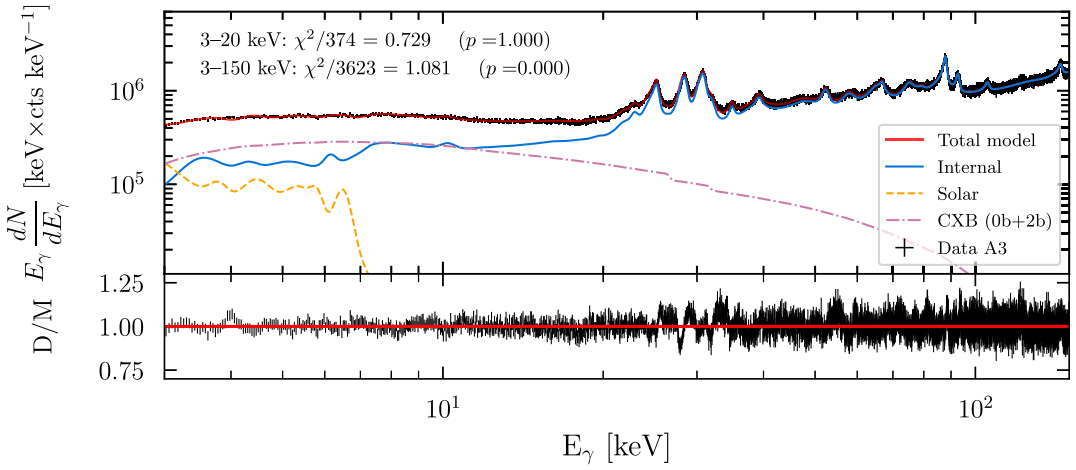

FIG. 10. Same as previous, for detector A3.

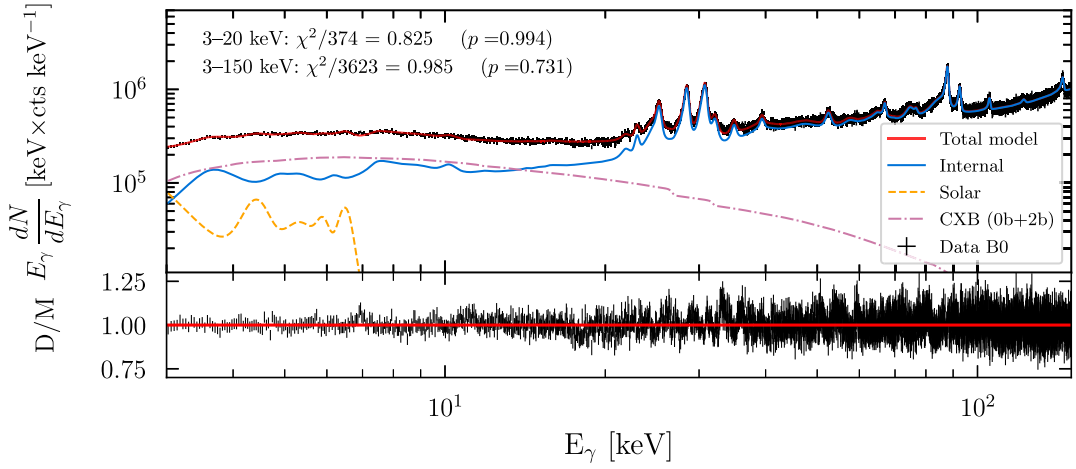

FIG. 11. Same as previous, for detector B0.

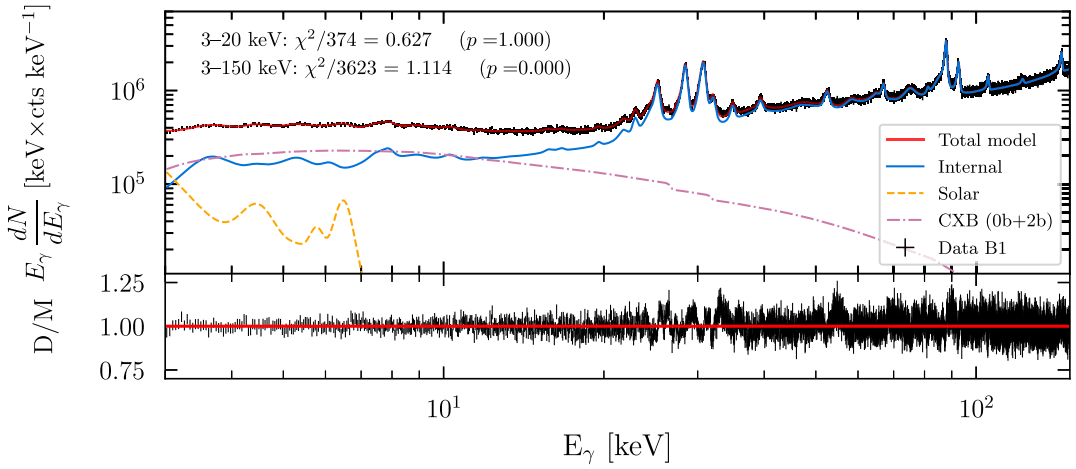

FIG. 12. Same as previous, for detector B1.

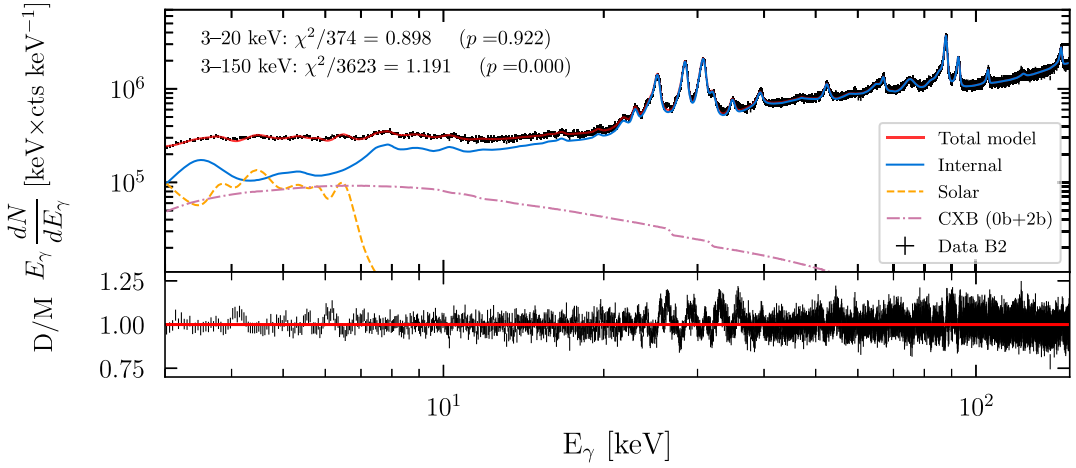

FIG. 13. Same as previous, for detector B2.

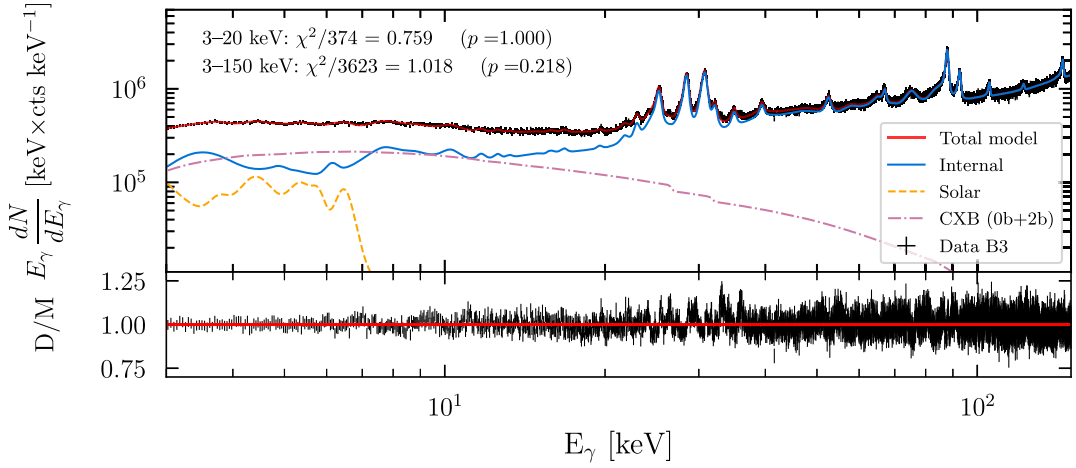

FIG. 14. Same as previous, for detector B3.

the energy range 3–20 keV is excellent, a result of the improved background modeling as well as the 2.5% systematic. The fit quality in the full 3–150-keV energy range is somewhat worse, resulting mainly from deviations around the bright detector fluorescence/activation lines between 20–40 keV. In both energy ranges, the χ^2 statistic is calculated with all detector line normalizations free.

[1] S. Funk, Indirect detection of dark matter with gamma rays, Proc. Natl. Acad. Sci. U.S.A. **112**, 12264 (2015).

[2] J. M. Gaskins, A review of indirect searches for particle dark matter, Contemp. Phys. **57**, 496 (2016).

[3] C. Pérez de los Heros, Status, challenges and directions in indirect dark matter searches, Symmetry **12**, 1648 (2020).

[4] T. Asaka, S. Blanchet, and M. Shaposhnikov, The νMSM, dark matter and neutrino masses, Phys. Lett. B **631**, 151 (2005).

[5] T. Asaka, M. Laine, and M. Shaposhnikov, Lightest sterile neutrino abundance within the νMSM, J. High Energy Phys. 01 (2007) 091; J. High Energy Phys. 02 (2015) 028.

[6] M. Shaposhnikov and I. Tkachev, The νMSM, inflation, and dark matter, Phys. Lett. B **639**, 414 (2006).

[7] M. Laine and M. Shaposhnikov, Sterile neutrino dark matter as a consequence of νMSM-induced lepton asymmetry, J. Cosmol. Astropart. Phys. 06 (2008) 031.

[8] S. Dodelson and L. M. Widrow, Sterile Neutrinos as Dark Matter, Phys. Rev. Lett. **72**, 17 (1994).

[9] X.-D. Shi and G. M. Fuller, A New Dark Matter Candidate: Nonthermal Sterile Neutrinos, Phys. Rev. Lett. **82**, 2832 (1999).

[10] A. Boyarsky, A. Neronov, O. Ruchayskiy, and M. Shaposhnikov, Constraints on sterile neutrinos as dark matter candidates from the diffuse x-ray background, Mon. Not. R. Astron. Soc. **370**, 213 (2006).

[11] A. Boyarsky, A. Neronov, O. Ruchayskiy, M. Shaposhnikov, and I. Tkachev, Where to Find a Dark Matter Sterile Neutrino?, Phys. Rev. Lett. **97**, 261302 (2006).

[12] A. Boyarsky, D. Malyshev, A. Neronov, and O. Ruchayskiy, Constraining dark matter properties with SPI, Mon. Not. R. Astron. Soc. **387**, 1345 (2008).

[13] C. R. Watson, J. F. Beacom, H. Yuksel, and T. P. Walker, Direct x-ray constraints on sterile neutrino warm dark matter, Phys. Rev. D **74**, 033009 (2006).

[14] H. Yuksel, J. F. Beacom, and C. R. Watson, Strong Upper Limits on Sterile Neutrino Warm Dark Matter, Phys. Rev. Lett. **101**, 121301 (2008).

[15] M. Loewenstein, A. Kusenko, and P. L. Biermann, New limits on sterile neutrinos from suzaku observations of the ursa minor dwarf spheroidal galaxy, Astrophys. J. **700**, 426 (2009).

[16] S. Riemer-Sørensen and S. H. Hansen, Decaying dark matter in draco, Astron. Astrophys. **500**, L37 (2009).

[17] S. Horiuchi, P. J. Humphrey, J. Onorbe, K. N. Abazajian, M. Kaplinghat, and S. Garrison-Kimmel, Sterile neutrino dark matter bounds from galaxies of the local group, Phys. Rev. D **89**, 025017 (2014).

[18] O. Urban, N. Werner, S. W. Allen, A. Simionescu, J. S. Kaastra, and L. E. Strigari, A suzaku search for dark matter emission lines in the x-ray brightest galaxy clusters, Mon. Not. R. Astron. Soc. **451**, 2447 (2015).

[19] T. Tamura, R. Iizuka, Y. Maeda, K. Mitsuda, and N. Y. Yamasaki, An x-ray spectroscopic search for dark matter in the perseus cluster with suzaku, Publ. Astron. Soc. Jpn. **67**, 23 (2015).

[20] E. Figueroa-Feliciano *et al.* (XQC Collaboration), Searching for keV sterile neutrino dark matter with x-ray microcalorimeter sounding rockets, Astrophys. J. **814**, 82 (2015).

[21] D. Iakubovskyi, E. Bulbul, A. R. Foster, D. Savchenko, and V. Sadova, Testing the origin of ~3.55 keV Line in individual galaxy clusters observed with XMM-newton, arXiv:1508.05186.

[22] K. C. Y. Ng, S. Horiuchi, J. M. Gaskins, M. Smith, and R. Preece, Improved limits on sterile neutrino dark matter using full-sky fermi gamma-ray burst monitor data, Phys. Rev. D **92**, 043503 (2015).

[23] F. A. Aharonian *et al.* (Hitomi Collaboration), Hitomi constraints on the 3.5 keV line in the perseus galaxy cluster, Astrophys. J. Lett. **837**, L15 (2017).

[24] N. Sekiya, N. Y. Yamasaki, and K. Mitsuda, A search for a keV signature of radiatively decaying dark matter with suzaku XIS observations of the x-ray diffuse background, Publ. Astron. Soc. Jpn. **68**, S31 (2016).

[25] C. Dessert, N. L. Rodd, and B. R. Safdi, The dark matter interpretation of the 3.5-keV line is inconsistent with Blank-Sky observations, Science **367**, 1465 (2020).

[26] F. Hofmann and C. Wegg, 7.1 keV sterile neutrino dark matter constraints from a deep chandra x-ray observation of the galactic bulge limiting window, Astron. Astrophys. **625**, L7 (2019).

[27] D. Sicilian, N. Cappelluti, E. Bulbul, F. Civano, M. Moscetti, and C. S. Reynolds, Probing the Milky Way's dark matter halo for the 3.5 keV line, Astrophys. J. **905**, 146 (2020).

[28] S. Bhargava, P. A. Giles, A. K. Romer, T. Jeltema, J. Mayers, A. Bermeo, M. Hilton, R. Wilkinson, C. Vergara, C. A. Collins, M. Manolopoulou, P. J. Rooney, S. Rosborough, K. Sabirli, J. P. Stott, E. Swann, and P. T. P. Viana, The XMM cluster survey: New evidence for the 3.5-keV feature in clusters is inconsistent with a dark matter origin, Mon. Not. R. Astron. Soc. **497**, 656 (2020).

[29] J. W. Foster, M. Kongsore, C. Dessert, Y. Park, N. L. Rodd, K. Cranmer, and B. R. Safdi, Deep Search for Decaying Dark Matter with XMM-Newton Blank-Sky Observations, Phys. Rev. Lett. **127**, 051101 (2021).

[30] E. M. Silich, K. Jahoda, L. Angelini, P. Kaaret, A. Zajczyk, D. M. LaRocca, R. Ringuette, and J. Richardson, A search for the 3.5 keV line from the Milky Way's dark matter halo with halosat, Astrophys. J. **916**, 2 (2021).
[31] E. Bulbul, M. Markevitch, A. Foster, R. K. Smith, M. Loewenstein, and S. W. Randall, Detection of an unidentified emission line in the stacked x-ray spectrum of galaxy clusters, Astrophys. J. **789**, 13 (2014).
[32] A. Boyarsky, O. Ruchayskiy, D. Iakubovskyi, and J. Franse, Unidentified Line in X-Ray Spectra of the Andromeda Galaxy and Perseus Galaxy Cluster, Phys. Rev. Lett. **113**, 251301 (2014).
[33] F. A. Harrison *et al.* (NuSTAR Collaboration), The nuclear spectroscopic telescope array (NuSTAR) high-energy x-ray mission, Astrophys. J. **770**, 103 (2013).
[34] S. Riemer-Sørensen *et al.*, Dark matter line emission constraints from NuSTAR observations of the bullet cluster, Astrophys. J. **810**, 48 (2015).
[35] A. Neronov, D. Malyshev, and D. Eckert, Decaying dark matter search with NuSTAR deep sky observations, Phys. Rev. D **94**, 123504 (2016).
[36] K. Perez, K. C. Y. Ng, J. F. Beacom, C. Hersh, S. Horiuchi, and R. Krivonos, Almost closing the νMSM sterile neutrino dark matter window with NuSTAR, Phys. Rev. D **95**, 123002 (2017).
[37] K. C. Y. Ng, B. M. Roach, K. Perez, J. F. Beacom, S. Horiuchi, R. Krivonos, and D. R. Wik, New constraints on sterile neutrino dark matter from NuSTAR M31 observations, Phys. Rev. D **99**, 083005 (2019).
[38] B. M. Roach, K. C. Y. Ng, K. Perez, J. F. Beacom, S. Horiuchi, R. Krivonos, and D. R. Wik, NuSTAR tests of sterile-neutrino dark matter: New galactic bulge observations and combined impact, Phys. Rev. D **101**, 103011 (2020).
[39] B. W. Grefenstette, W. R. Cook, F. A. Harrison, T. Kitaguchi, K. K. Madsen, Miyasaka H, and S. N. Pike, Pushing the limits of NuSTAR detectors, in *High Energy, Optical, and Infrared Detectors for Astronomy VIII*, edited by A. D. Holland and J. Beletic, International Society for Optics and Photonics Vol. 10709 (SPIE, Austin, Texas, USA, 2018), p. 705.
[40] K. K. Madsen *et al.*, Calibration of the NuSTAR high energy focusing x-ray telescope, Astrophys. J. Suppl. Ser. **220**, 8 (2015).
[41] K. K. Madsen, K. Forster, B. W. Grefenstette, F. A. Harrison, and H. Miyasaka, Effective area calibration of the Nuclear Spectroscopic Telescope Array, J. Astron. Telesc. Instrum. Syst. **8**, 034003 (2022).
[42] D. R. Wik *et al.*, NuSTAR observations of the bullet cluster: Constraints on inverse compton emission, Astrophys. J. **792**, 48 (2014).
[43] R. Krivonos, D. Wik, B. Grefenstette, K. Madsen, K. Perez, S. Rossland, S. Sazonov, and A. Zoglauer, NuSTAR measurement of the cosmic x-ray background in the 3–20 keV energy band, Mon. Not. R. Astron. Soc. **502**, 3966 (2021).
[44] H. Zhao, Analytical models for galactic nuclei, Mon. Not. R. Astron. Soc. **278**, 488 (1996).
[45] J. F. Navarro, C. S. Frenk, and S. D. M. White, A universal density profile from hierarchical clustering, Astrophys. J. **490**, 493 (1997).
[46] M. Pato, F. Iocco, and G. Bertone, Dynamical constraints on the dark matter distribution in the Milky Way, J. Cosmol. Astropart. Phys. 12 (2015) 001.
[47] E. V. Karukes, M. Benito, F. Iocco, R. Trotta, and A. Geringer-Sameth, Bayesian reconstruction of the Milky Way dark matter distribution, J. Cosmol. Astropart. Phys. 09 (2019) 046.
[48] P. F. de Salas, K. Malhan, K. Freese, K. Hattori, and M. Valluri, On the estimation of the local dark matter Density using the rotation curve of the Milky Way, J. Cosmol. Astropart. Phys. 10 (2019) 037.
[49] P. F. de Salas and A. Widmark, Dark matter local density determination: Recent observations and future prospects, Rep. Prog. Phys. **84**, 104901 (2021).
[50] Y. Sofue, Rotation curve of the Milky Way and the dark matter density, Galaxies **8**, 37 (2020).
[51] M. Cautun *et al.*, The Milky Way total mass profile as inferred from gaia DR2, Mon. Not. R. Astron. Soc. **494**, 4291 (2020).
[52] V. V. Bobylev and A. T. Bajkova, A new estimate of the best value for the solar galactocentric distance, Astronomy Reports **65**, 498 (2021).
[53] F. Civano *et al.*, The NuSTAR extragalactic surveys: Overview and catalog from the COSMOS field, Astrophys. J. **808**, 185 (2015).
[54] M. Davis *et al.*, The all-wavelength extended groth strip international survey (AEGIS) data sets, Astrophys. J. Lett. **660**, L1 (2007).
[55] J. R. Mullaney *et al.*, The NuSTAR extragalactic surveys: Initial results and catalog from the extended chandra deep field south, Astrophys. J. **808**, 184 (2015).
[56] A. Masini *et al.*, The NuSTAR extragalactic surveys: Source catalog and the compton-thick fraction in the UDS field, Astrophys. J. Suppl. Ser. **235**, 17 (2018).
[57] K. K. Madsen, F. E. Christensen, W. W. Craig, K. W. Forster, B. W. Grefenstette, F. A. Harrison, H. Miyasaka, and V. Rana, Observational artifacts of nuclear spectroscopic telescope array: Ghost rays and stray light, J. Astron. Telesc. Instrum. Syst. **3**, 044003 (2017).
[58] D. E. Gruber, J. L. Matteson, L. E. Peterson, and G. V. Jung, The spectrum of diffuse cosmic hard x-rays measured with HEAO-1, Astrophys. J. **520**, 124 (1999).
[59] J. M. Dickey and F. J. Lockman, HI in the Galaxy, Annu. Rev. Astron. Astrophys. **28**, 215 (1990).
[60] P. M. W. Kalberla, W. B. Burton, D. Hartmann, E. M. Arnal, E. Bajaja, R. Morras, and W. G. L. Pöppel, The Leiden/Argentine/Bonn (LAB) survey of galactic HI: Final data release of the combined LDS and IAR surveys with improved stray-radiation corrections, Astron. Astrophys. **440**, 775 (2005).
[61] J. Wilms, A. Allen, and R. McCray, On the absorption of x-rays in the interstellar medium, Astrophys. J. **542**, 914 (2000).
[62] E. Anders and N. Grevesse, Abundances of the elements: Meteroritic and solar, Geochim. Cosmochim. Acta **53**, 197 (1989).
[63] B. M. Roach *et al.*, nustar-blanksky, https://github.com/roachb/nustar-blanksky.
[64] B. W. Grefenstette *et al.*, in review at JATIS.

[65] E. Churazov, S. Sazonov, R. Sunyaev, and M. Revnivtsev, Earth x-ray albedo for cosmic x-ray background radiation in the 1–1000 keV band, Mon. Not. R. Astron. Soc. **385**, 719 (2008).

[66] I. G. Hannah *et al.*, The first x-ray imaging spectroscopy of quiescent solar active regions with NuSTAR, Astrophys. J. Lett. **820**, L14 (2016).

[67] L. Glesener, S. Krucker, I. G. Hannah, H. Hudson, B. W. Grefenstette, S. M. White, D. M. Smith, and A. J. Marsh, NuSTAR hard x-ray observation of a sub-A class solar flare, Astrophys. J. **845**, 122 (2017).

[68] P. J. Wright *et al.*, Microflare heating of a solar active region observed with NuSTAR, Hinode/XRT, and SDO/AIA, Astrophys. J. **844**, 132 (2017).

[69] M. Kuhar, S. Krucker, L. Glesener, I. G. Hannah, B. W. Grefenstette, D. M. Smith, H. S. Hudson, and S. M. White, NuSTAR detection of x-ray heating events in the quiet sun, Astrophys. J. Lett. **856**, L32 (2018).

[70] G. Cowan, K. Cranmer, E. Gross, and O. Vitells, Asymptotic formulae for likelihood-based tests of new physics, Eur. Phys. J. C **71**, 1554 (2011); Eur. Phys. J. C **73**, 2501(E) (2013).

[71] S. Algeri, J. Aalbers, K. D. Morå, and J. Conrad, Searching for new phenomena with profile likelihood ratio tests, Nat. Rev. Phys. **2**, 245 (2020).

[72] J. W. Foster, N. L. Rodd, and B. R. Safdi, Revealing the dark matter halo with axion direct detection, Phys. Rev. D **97**, 123006 (2018).

[73] P. Arias, D. Cadamuro, M. Goodsell, J. Jaeckel, J. Redondo, and A. Ringwald, WISPy Cold Dark Matter, J. Cosmol. Astropart. Phys. 06 (2012) 013.

[74] I. G. Irastorza and J. Redondo, New experimental approaches in the search for axion-like particles, Prog. Part. Nucl. Phys. **102**, 89 (2018).

[75] E. Aprile *et al.* (XENON Collaboration), Excess electronic recoil events in XENON1T, Phys. Rev. D **102**, 072004 (2020).

[76] F. Takahashi, M. Yamada, and W. Yin, XENON1T Excess from Anomaly-Free Axionlike Dark Matter and Its Implications for Stellar Cooling Anomaly, Phys. Rev. Lett. **125**, 161801 (2020).

[77] Glen Cowan, Kyle Cranmer, Eilam Gross, and Ofer Vitells, Power-constrained limits, arXiv:1105.3166.

[78] R. Shrock, Decay $L^0 \to \nu_l \gamma$ in gauge theories of weak and electromagnetic interactions, Phys. Rev. D **9**, 743 (1974).

[79] P. B. Pal and L. Wolfenstein, Radiative decays of massive neutrinos, Phys. Rev. D **25**, 766 (1982).

[80] K. N. Abazajian, Technical Comment on "The dark matter interpretation of the 3.5-keV line is inconsistent with Blank-Sky observations", arXiv:2004.06170.

[81] A. Boyarsky, D. Malyshev, O. Ruchayskiy, D. Savchenko, Technical comment on the paper of Dessert et al. "The dark matter interpretation of the 3.5 keV line is inconsistent with Blank-Sky observations", arXiv:2004.06601.

[82] C. Dessert, N. L. Rodd, B. R. Safdi Response to a Comment on Dessert et al. "The dark matter interpretation of the 3.5 keV line is inconsistent with Blank-Sky observations", Phys. Dark Universe **30**, 100656 (2020).

[83] A. Neronov and D. Malyshev, Toward a full test of the νMSM sterile neutrino dark matter model with athena, Phys. Rev. D **93**, 063518 (2016).

[84] L. Canetti, M. Drewes, and M. Shaposhnikov, Sterile Neutrinos as the Origin of Dark and Baryonic Matter, Phys. Rev. Lett. **110**, 061801 (2013).

[85] L. Canetti, M. Drewes, T. Frossard, and M. Shaposhnikov, Dark matter, baryogenesis and neutrino oscillations from right handed neutrinos, Phys. Rev. D **87**, 093006 (2013).

[86] T. Venumadhav, F.-Y. Cyr-Racine, K. N. Abazajian, and C. M. Hirata, Sterile neutrino dark matter: Weak interactions in the strong coupling epoch, Phys. Rev. D **94**, 043515 (2016).

[87] P. D. Serpico and G. G. Raffelt, Lepton asymmetry and primordial nucleosynthesis in the era of precision cosmology, Phys. Rev. D **71**, 127301 (2005).

[88] J. F. Cherry and S. Horiuchi, Closing in on resonantly produced sterile neutrino dark matter, Phys. Rev. D **95**, 083015 (2017).

[89] A. Boyarsky, O. Ruchayskiy, and M. Shaposhnikov, The role of sterile neutrinos in cosmology and astrophysics, Annu. Rev. Nucl. Part. Sci. **59**, 191 (2009).

[90] J. Ghiglieri and M. Laine, Improved determination of sterile neutrino dark matter spectrum, J. High Energy Phys. 11 (2015) 171.

[91] A. Boyarsky, M. Drewes, T. Lasserre, S. Mertens, and O. Ruchayskiy, Sterile neutrino dark matter, Prog. Part. Nucl. Phys. **104**, 1 (2019).

[92] K. N. Abazajian, Sterile neutrinos in cosmology, Phys. Rep. **711–712**, 1 (2017).

[93] A. Schneider, Astrophysical constraints on resonantly produced sterile neutrino dark matter, J. Cosmol. Astropart. Phys. 04 (2016) 059.

[94] A. Dekker, S. Ando, C. A. Correa, and K. C. Y. Ng, Warm dark matter constraints using Milky~Way satellite observations and subhalo evolution modeling, Phys. Rev. D **106**, 123026 (2022).

[95] J. Baur, N. Palanque-Delabrouille, C. Yeche, A. Boyarsky, O. Ruchayskiy, É. Armengaud, and J. Lesgourgues, Constraints from Ly-α Forests on non-thermal dark matter including resonantly-produced sterile neutrinos, J. Cosmol. Astropart. Phys. 12 (2017) 013.

[96] C. Yèche, N. Palanque-Delabrouille, Julien Baur, and H. du Mas des Bourboux, Constraints on neutrino masses from Lyman-alpha forest power spectrum with BOSS and XQ-100, J. Cosmol. Astropart. Phys. 06 (2017) 047.

[97] A. Garzilli, A. Magalich, T. Theuns, C. S. Frenk, C. Weniger, O. Ruchayskiy, and A. Boyarsky, The Lyman-α forest as a diagnostic of the nature of the dark matter, Mon. Not. R. Astron. Soc. **489**, 3456 (2019).

[98] N. Palanque-Delabrouille, C. Yèche, N. Schöneberg, J. Lesgourgues, M. Walther, S. Chabanier, and E. Armengaud, Hints, neutrino bounds and WDM constraints from SDSS DR14 Lyman-α and planck full-survey data, J. Cosmol. Astropart. Phys. 04 (2020) 038.

[99] A. Schneider, Structure formation with suppressed small-scale perturbations, Mon. Not. R. Astron. Soc. **451**, 3117 (2015).

[100] E. O. Nadler *et al.* (DES Collaboration), Milky Way Satellite Census. III. Constraints on Dark Matter Properties

from Observations of Milky Way Satellite Galaxies, Phys. Rev. Lett. **126**, 091101 (2021).
[101] O. Newton, M. Leo, M. Cautun, A. Jenkins, C. S. Frenk, M. R. Lovell, J. C. Helly, A. J. Benson, and S. Cole, Constraints on the properties of warm dark matter using the satellite galaxies of the Milky Way, J. Cosmol. Astropart. Phys. 08 (2021) 062.
[102] A. Kusenko, Sterile Neutrinos, Dark Matter, and the Pulsar Velocities in Models with a Higgs Singlet, Phys. Rev. Lett. **97**, 241301 (2006).
[103] A. Adulpravitchai and M. A. Schmidt, A fresh look at keV sterile neutrino dark matter from frozen-in scalars, J. High Energy Phys. 01 (2015) 006.
[104] M. Drewes and J. U Kang, Sterile neutrino dark matter production from scalar decay in a thermal bath, J. High Energy Phys. 05 (2016) 051.
[105] P. Predehl *et al.* (eROSITA Collaboration), The eROSITA x-ray telescope on SRG, Astron. Astrophys. **647**, A1 (2021).
[106] M. Pavlinsky *et al.*, The ART-XC telescope on board the SRG observatory, Astron. Astrophys. **650**, A42 (2021).
[107] A. J. F. Hubbard *et al.*, Design and status of the micro-X microcalorimeter sounding rocket, J. Phys. Conf. Ser. **1342**, 012096 (2020).
[108] L. Angelini *et al.* (XRISM Science Team), Science with the x-ray imaging and spectroscopy mission (XRISM), arXiv:2003.04962.
[109] K. Nandra *et al.*, The hot and energetic universe: A white paper presenting the science theme motivating the Athena + mission, arXiv:1306.2307.
[110] R. Mushotzky (AXIS Team), AXIS: A probe class next generation high angular resolution x-ray imaging satellite, Proc. SPIE Int. Soc. Opt. Eng. **10699**, 1069929 (2018).
[111] S. N. Zhang *et al.* (eXTP Collaboration), eXTP—enhanced x-ray timing and polarimetry mission, Proc. SPIE Int. Soc. Opt. Eng. **9905**, 99051Q (2016).
[112] K. Madsen *et al.*, HEX-P: The high-energy x-ray probe, Bull. Am. Astron. Soc. **51** (2019).
[113] S. Allen *et al.* (Lynx Team), The Lynx mission concept study interim report, arXiv:1809.09642.
[114] E. G. Speckhard, K. C. Y. Ng, J. F. Beacom, and R. Laha, Dark Matter Velocity Spectroscopy, Phys. Rev. Lett. **116**, 031301 (2016).
[115] A. Caputo, M. Regis, and M. Taoso, Searching for sterile neutrino with x-ray intensity mapping, J. Cosmol. Astropart. Phys. 03 (2020) 001.
[116] M. R. Lovell, D. Iakubovskyi, D. Barnes, S. Bose, C. S. Frenk, T. Theuns, and W. A. Hellwing, Simulating the dark matter decay signal from the perseus galaxy cluster, Astrophys. J. Lett. **875**, L24 (2019).
[117] D. Zhong, M. Valli, and K. N. Abazajian, Near to long-term forecasts in x-ray and gamma-ray bands: Are we entering the era of dark matter astronomy?, Phys. Rev. D **102**, 083008 (2020).
[118] A. Dekker, E. Peerbooms, F. Zimmer, K. C. Y. Ng, and S. Ando, Searches for sterile neutrinos and axionlike particles from the galactic halo with eROSITA, Phys. Rev. D **104**, 023021 (2021).